Check for updates

Novel easily separable core–shell Fe$_3$O$_4$/PVP/ZIF-8 nanostructure adsorbent: optimization of phosphorus removal from Fosfomycin pharmaceutical wastewater†

Mai O. Abdelmigeed, [ID] [a] Ahmed H. Sadek [ID] [bc] and Tamer S. Ahmed [ID] *[ab]

A new easily separable core–shell Fe$_3$O$_4$/PVP/ZIF-8 nanostructure adsorbent was synthesized and then examined for removal of Fosfomycin antibiotic from synthetic pharmaceutical wastewater. The removal process of Fosfomycin was expressed through testing the total phosphorus (TP). A response surface model (RSM) for Fosfomycin adsorption (as mg-P L^{-1}) was used by carrying out the experiments using a central composite design. The adsorption model showed that Fosfomycin adsorption is directly proportional to core–shell Fe$_3$O$_4$/PVP/ZIF-8 nanostructure adsorbent dosage and time, and indirectly to initial Fosfomycin concentration. The removal increased by decreasing the pH to 2. The Fosfomycin removal was done at room temperature under an orbital agitation speed of 250 rpm. The adsorption capacity of core–shell Fe$_3$O$_4$/PVP/ZIF-8 nanostructure adsorbent reached around 1200 mg-P g^{-1}, which is significantly higher than other MOF adsorbents reported in the literature. The maximum Langmuir adsorption capacity of the adsorbent for Fosfomycin was 126.58 mg g^{-1} and Fosfomycin adsorption behavior followed the Freundlich isotherm ($R^2 = 0.9505$) in the present study. The kinetics was best fitted by the pseudo-second-order model ($R^2 = 0.9764$). The RSM model was used for the adsorption process in different target modes.

1 Introduction

Currently, pharmaceutical waste is ubiquitous and lead to heavily contaminated ecosystems, which directly and harmfully affect both humans and environmental systems.[1] Pharmaceuticals are detected in tap water, ocean water, sediments, soil,[2] and drinking water,[3] as well as surface and groundwater.[4] Pharmaceuticals end up accumulating in the soil, surface waters, and eventually in ground and drinking water after their excretion in unmetabolized form or as active metabolites. The main sources are domestic from humans or animals *via* urine or feces, industrial, and pharmaceutical wastewater.[5] On the other hand, veterinary pharmaceuticals directly contaminate soil *via* manure and surface and ground waters that run off from fields.[6]

Pharmaceuticals are mainly synthesized to have a physiological effect in trace concentrations on humans and animals. The key reason behind considering pharmaceuticals as

aChemical Engineering Department, Faculty of Engineering, Cairo University, Giza, 12613, Egypt. E-mail: tamer.s.ahmed@cu.edu.eg

bEnvironmental Engineering Program, Zewail City of Science, Technology and Innovation, 6th October City, Giza, 12578, Egypt

cSanitary and Environmental Engineering Research Institute, Housing and Building National Research Center (HBRC), Dokki, 11511, Giza, Egypt

† Electronic supplementary information (ESI) available. See https://doi.org/10.1039/d2ra00936f

pollutants is their persistence against biological degradation and biological activity. They retain their chemical structure long enough to do their therapeutic work. Because of their continuous input, they could remain in the environment for a long time and their presence is considered dangerous in both low and high concentrations.[7] These active ingredients are selected or designed because of their activity against organisms. Due to its low degradability, 80% of these substances are rawly discharged by excretion and flushed into the sewers to the sewage plants. This leads to the growth of bacterial resistance, which results in difficulties in treating common illnesses.[8] Consequently, as an example, many countries put restrictions on discharge limits for phosphates as 0.5–1.0 mg L^{-1} in Japan,[9] 1–2 mg L^{-1} in France,[10] and 0.5–1.0 mg L^{-1} in USA.[10] In particular, a new mandate of even lower phosphate concentrations of 0.05 mg L^{-1} and 0.01 mg L^{-1} was respectively suggested by Europe and North America.[11]

One of the most wide-spectrum antibiotics is Fosfomycin (1R-2S-epoxypropyl phosphonic acid). At first, Fosfomycin was synthesized from a fermentation broth of *Streptomyces fradiae*, but now it can be synthesized using chemical synthesis. The chemical synthesis process of Fosfomycin pharmaceutical produces highly contaminated Fosfomycin wastewater, *i.e.*, the residual mother liquor effluent. A variety of organic phosphorus (OP) intermediates, by-products, and finished products

(epoxypropenyl phosphonic acid, propenyl phosphonic acid, propargyl phosphonic acid, ..., *etc.* as well as some raw materials and solvents like EDTA, anilines, and alcohols) are considered as the main pollutants in the Fosfomycin wastewater. The main disadvantage of the highly contaminated wastewater with antibiotic OP compounds is being toxic, non-biodegradable, and recalcitrant to the biological culture. Accordingly, the development of effective methods for such antibiotic-contaminant wastewater treatment becomes urgent.[12]

Several pollutants like phosphates, methylene blue, Cu(II), and Cd(II) were removed by using nano-adsorbent materials such as zero-valent iron nanoparticles in both pristine and encapsulated forms, magnetite nanoparticles, ..., *etc.*[13–18] Recently, sustainable green nano adsorbents,[19] and sustainable photocatalytic membranes[20] have been used for water and wastewater remediation of pharmaceuticals. Metal–organic frameworks (MOFs) attracted large attention due to their applications in energy generation,[21] catalytic degradation,[22] gas storage,[23,24] gas/heavy metal adsorption,[25–27] chemical catalysis,[28] and environmental remediation.[29–31] Even though the bare MOFs can be used as adsorbents, nevertheless, certain disadvantages impede the removal efficiencies for pollutants due to weaker adsorption affinity resulting from their large amount of void space and the limited unsaturated metallic centers.[32,33] That is why even larger attention is focused on the fabrication and application of various MOFs-based composites for example MOFs/carbon materials (MOFs-C). In comparison with the individual MOF species, the performances of MOFs-C hybrids were remarkably improved.[34–36]

In the current work, the core–shell magnetite/polyvinylpyrrolidone/zeolitic imidazolate framework-8 (Fe$_3$O$_4$/PVP/ZIF-8) nanostructure was fabricated *via in situ* growth of ZIF-8 on Fe$_3$O$_4$ nanoparticles, while the PVP act as a binder. The prepared core–shell Fe$_3$O$_4$/PVP/ZIF-8 nanostructure has undergone many characterization studies using FTIR, TEM, SEM-EDX mapping, XRD, and N$_2$ gas adsorption–desorption analyses to confirm the structure and morphology of synthesized nanostructure. The nanostructure was then evaluated for the efficient removal of total phosphorus from Fosfomycin pharmaceutical wastewater. The current study encompasses three specific objectives: (i) preparation of core–shell Fe$_3$O$_4$/PVP/ZIF-8 nanostructure adsorbent with full characterization; (ii) optimization of the performance of the core–shell Fe$_3$O$_4$/PVP/ZIF-8 nanostructure adsorbent for Fosfomycin adsorption expressed as total phosphorus, stability, and regeneration ability; (iii) determination the appropriate kinetics and isotherms models for the adsorption process.

2 Materials and methods

2.1 Materials

Methanol (CH$_3$OH, assay 99.9%), and sodium hydroxide pellets (NaOH, purified, assay ≥97%) (both in analytical grade) were supplied from El-Nasr Pharmaceutical Chemicals Company, Egypt. Ferrous chloride hydrated (FeCl$_2$, 98%, extra pure), ferric chloride anhydrous (FeCl$_3$, 98%, extra pure), 2-methyl
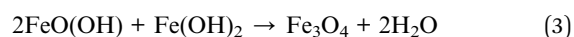
imidazole (CH$_3$C$_3$H$_2$N$_2$H), and zinc nitrate hexahydrate (Zn(NO$_3$)$_2$·6H$_2$O, purified) were supplied from Loba Chemicals Company, India. Polyvinylpyrrolidone (PVP) (K30) (PVP, molar mass 44 000–54 000 (g mol^{-1}), assay (from N) 12.0–12.8%, BioChemica) was purchased from Panreac AppliChem. Concentrated HCl (analytical grades, El-Nasr Pharmaceutical Chemicals Company, Egypt) and NaOH were used to adjust the pH of solutions. All chemicals were used without further purification. Distilled water was used for the preparation of all the solutions.

2.2 Preparation of synthetic Fosfomycin pharmaceutical wastewater

A 5.631 g of Fosfomycin trometamol antibiotic equivalent to 3.0 g Fosfomycin was dissolved in 50 mL distilled water giving 899 g-P L^{-1}. This solution was then diluted to the desired concentrations (900 mg-P L^{-1}, 465 mg-P L^{-1}, and 30 mg-P L^{-1}) by successive dilutions.

2.3 Preparation of core–shell Fe$_3$O$_4$/PVP/ZIF-8 nanostructure adsorbent

2.3.1 Synthesis of magnetite nanoparticles. Magnetite nanoparticles were synthesized by the co-precipitation technique using FeCl$_2$ (0.1 M)/FeCl$_3$ (0.2 M) aqueous solutions with the addition of NaOH (0.1 M) while stirring was continued for 1 h. The mixture was then washed and centrifuged (6000 rpm) for 15 min to collect the produced solid magnetite nanoparticles, which were dried in an oven at 110 °C for 24 h.[37,38] Eqn (1)–(3) represent the synthesis steps for the preparation of magnetite nanoparticles.

$$FeCl_3 + 3NaOH \rightarrow FeO(OH) + 3NaCl + H_2O \quad (1)$$

$$FeCl_2 + 2NaOH \rightarrow Fe(OH)_2 + 2NaCl \quad (2)$$

$$2FeO(OH) + Fe(OH)_2 \rightarrow Fe_3O_4 + 2H_2O \quad (3)$$

2.3.2 Stabilization of magnetite with PVP. Polyvinylpyrrolidone (PVP) is an ionic polymer and was used to modify the surface charge of the magnetite nanoparticles to adsorb Zn^{2+} cations to initiate nucleation, deposition, and growth of the ZIF-8 network on the magnetite surface. PVP solution was prepared in 40 mL at a concentration of (2.5 w/w%) PVP/H$_2$O. One gram of magnetite nanoparticles was added to 10 mL of the aforementioned PVP solution. This mixture was sonicated for 15 min at 50 °C followed by shaking at 150 rpm for 100 min at room temperature. The mixture was then centrifuged (6000 rpm) for 15 min to collect the produced PVP–magnetite nanoparticles.[39]

2.3.3 ZIF-8 network growth onto magnetite/PVP. ZIF-8 was synthesized by preparing two solutions of Zn(NO$_3$)$_2$·6H$_2$O (2.932 g) in 200 mL of methanol (solution A) and 2-methyl imidazole (6.488 g) in another 200 mL of methanol (solution B). Then, the PVP–magnetite nanoparticles were added to solution B while the stirring continued for 1 h using a mechanical agitator (Hei-torque 400, Heidolph, Germany).[37,38] Afterward,

solution A was added to solution B under continuous stirring. Immediately, the growth of the ZIF-8 network begins to start while the stirring continued for another 1 h. After that, the mixture was centrifuged (6000 rpm) for 15 min to collect the produced core–shell Fe_3O_4/PVP/ZIF-8 nanostructure adsorbent in its final form, which was dried in an oven at 105 °C for 24 h.

2.4 Characterization of synthesized core–shell Fe_3O_4/PVP/ZIF-8 nanostructure adsorbent

The prepared core–shell Fe_3O_4/PVP/ZIF-8 nanostructure adsorbent was characterized using different tools to characterize its structure and morphological properties completely. Fourier infrared transform spectroscopy (FTIR, Jasco FTIR-4100 spectrophotometer, Japan) was used to reveal the functional groups and the successful establishment of core–shell structure, besides the studying effect of different adsorption conditions on the integrity of core–shell Fe_3O_4/PVP/ZIF-8 in the range of 500–4000 cm^{-1}.

TEM analysis was performed using a transmission electron microscope (TEM, JEOL, TEM-2100, USA) operated at a potential of 20 kV for further demonstration of the core–shell structure and the size of core and shell thickness. Before the TEM inspection, a desirable amount of core–shell Fe_3O_4/PVP/ZIF-8 nanostructure adsorbent powder was dispersed in ethanol and sonicated with an ultrasonic cleaner (Elma, Singen, Germany) for 15 min. Then, a few drops of the core–shell Fe_3O_4/PVP/ZIF-8 nanostructure adsorbent suspension was deposited onto the carbon-coated copper grid and allowed to dry at room temperature.

The shape and elemental composition of synthesized core–shell Fe_3O_4/PVP/ZIF-8 nanostructure adsorbent were investigated using a scanning electron microscope (SEM, JSM-6701F Plus, JEOL, USA) equipped with energy-dispersive X-ray spectroscopy (EDX) at an accelerating voltage of 20 kV.

X-ray diffractometer (XRD, D8-Discover, Bruker, USA) was used to examine the crystallinity and stability of core–shell Fe_3O_4/PVP/ZIF-8 nanostructure adsorbent before and after hydration by Fosfomycin antibiotic with 2θ ranging from 10° to 80° at a wavelength of CuKα radiation ($\lambda = 1.5406$ Å) that operates at 40 kV and 40 mA. Finally, the specific surface area and porosity of synthesized core–shell Fe_3O_4/PVP/ZIF-8 nanostructure adsorbent were obtained through the N_2 gas adsorption–desorption technique using Brunauer–Emmett–Teller (BET) analyzer (NOVA touch 4LX [s/n:17016062702], Quantachrome, USA) and according to Barrett–Joyner–Halenda (BJH) theory.

2.5 Fosfomycin removal experiments and analysis methods

Eighteen batch mode experiments (100 mL each) were carried out in an incubator shaker at different initial Fosfomycin concentrations (30, 465, and 900 mg-P L^{-1}), adsorbent dosages (0.1, 0.3, 0.5 g/100 mL), and contact time (30, 105, and 180 min). All the runs were conducted at room temperature 25 °C with 250 rpm using an orbital incubator shaker (Labtech LSI 3016R, Korea). The core–shell Fe_3O_4/PVP/ZIF-8 nanostructure adsorbent was separated using a strong magnet. The concentrations

of phosphorous-containing Fosfomycin were determined by performing a total phosphorous (TP) test as an indication of the existence of residual concentrations of Fosfomycin antibiotics in the solutions. Firstly, after the separation step, the samples were digested through the persulfate digestion method.[40] Later, the digested samples were measured by the stannous chloride method at $\lambda = 690$ nm according to standard methods for the examination of water and wastewater using T80, UV-Vis spectrophotometer (PG Instruments, UK).[40] Fig. 1 illustrates the coating step of magnetite nanoparticles by PVP and ZIF-8 growth, additionally to the mechanism of Fosfomycin adsorption on the surface of core–shell Fe_3O_4/PVP/ZIF-8 nanostructure.

2.6 Response surface methodology (RSM)

Response surface methodology (RSM) is made of mathematical and applied math techniques (statistical techniques) to produce a purposeful relationship between independent variables χ_n which are adsorbent dosage, Fosfomycin initial concentration, and contact time in this study *versus* a response y which is % removal of Fosfomycin. This relationship is approximated by a low degree polynomial model of the shape

$$y = f(x) + \varepsilon \qquad (4)$$

where $\chi_n, f(x)$ is a vector operate of m components that are made up of powers & cross products of powers χ_n up to a definite degree denoted by κ (≥ 1). γ is a vector of m unknown constant coefficients & ε is an unspecified experimental error assumed to possess a zero mean.[41]

2.7 Adsorption kinetics and isotherm

2.7.1 Kinetics models. To investigate the adsorption kinetics, pseudo-first-order, pseudo-second-order, and intra-particle diffusion linear kinetic models were applied for the estimation of rate constants.[42,43] Pseudo-first-order expression was employed as in eqn (5):

$$\log(q_e - q_t) = \log q_e - \frac{k_1}{2.303}t \qquad (5)$$

where k_1 is the first-order rate constant of adsorption (min^{-1}); q_e (mg g^{-1}) and q_t (mg g^{-1}) are the amount of phosphorus adsorbed at equilibrium and at time t, respectively. The values of k_1 and q_e can be obtained from the slope and the intercept of a linear straight-line plot of $\log(q_e - q_t)$ *versus* t. The pseudo-second-order equation is shown in eqn (6):

$$\frac{t}{q_t} = \frac{1}{k_2 q_e^2} + \frac{1}{q_e}t \qquad (6)$$

where q_e (mg g^{-1}) and q_t (mg g^{-1}) are the amount of phosphorus adsorbed at equilibrium and time t respectively; and k_2 is the rate constant of the pseudo-second-order model (g mg^{-1} min^{-1}). The value of the k_2 and q_e can be obtained from the linear t/q_t *vs.* t plot. The intra-particle diffusion equation can be written as shown in eqn (7):

$$q_t = k_p t^{0.5} + c \qquad (7)$$

where q_t (mg g^{-1}) is the amount of phosphorus adsorbed at time t; k_p is the rate constant of the intra-particle diffusion model (mg g^{-1} min$^{-0.5}$); c is the intra-particle diffusion model's constant (mg g^{-1}). The value of the k_p and c can be obtained from the linear q_t *vs.* $t^{0.5}$ plot.

2.7.2 Isotherm models. Langmuir, Freundlich, Temkin, and Dubinin–Radushkevich isotherms are the most frequently used models to analyze experimental observations.[43,44] These four non-linear isotherm models (eqn (8)–(11)) were applied to obtain the adsorption isotherm constants.

Langmuir equation:

$$\frac{c_e}{q_e} = \frac{1}{q_m}c_e + \frac{1}{q_m b} \quad (8)$$

Freundlich equation:

$$\log(q_e) = \log(K_f) + \frac{1}{n}\log(C_e) \quad (9)$$

Temkin equation:

$$q_e = B_1 \ln(k_t) + B_1 \ln(C_e) \quad (10)$$

Dubinin–Radushkevich equation:

$$\ln(q_e) = \ln(q_m) - \beta\varepsilon^2 \quad (11)$$

where q_e (mg g^{-1}) is the specific amount of adsorbate (phosphorus), and C_e (mg-P L^{-1}) is the adsorbate concentration in the liquid phase at equilibrium. The constants b (L mg^{-1}) and q_{max} (mg g^{-1}) of the Langmuir isotherm are indicative of adsorption energy and adsorption density, respectively. K_F (mg g^{-1}) and n (dimensionless) are Freundlich constants and indicate the total adsorption capacity and intensity of adsorption, respectively. The constants B_1 (mg g^{-1}) is Temkin constant, k_t is Temkin isotherm constant (L g^{-1}). β is Dubinin–Radushkevich constant (mol^2 J^{-2}), and ε is Polanyi potential (J mol^{-1}), respectively. ε can be calculated from eqn (12):

$$\varepsilon = RT \ln\left(1 + \frac{1}{C_e}\right) \quad (12)$$

where R is universal gas constant (J mol^{-1} K^{-1}), T is temperature (K), and C_e (mg-P L^{-1}) is the adsorbate concentration in the liquid phase at equilibrium.

The Langmuir equation is also used to obtain R_L, the separation factor, from the following expression: $R_L = \frac{1}{1 + K_L C_0}$ in which C_0 (mg-P L^{-1}) is the initial concentration of phosphorus in the solution. If $0 < R_L < 1$ then a favorable adsorption situation can be assumed, while $R_L > 1$ indicates an unfavorable adsorption, while $R_L = 1$ and $R_L = 0$ indicate a linear and irreversible adsorption isotherm, respectively.[45]

2.8 Regeneration experiments

The regeneration experiments of core–shell Fe$_3$O$_4$/PVP/ZIF-8 nanostructure adsorbent was done by washing the used core–shell Fe$_3$O$_4$/PVP/ZIF-8 nanostructure adsorbent with distillate water followed by heating at 110 °C for 24 h. The dried core–
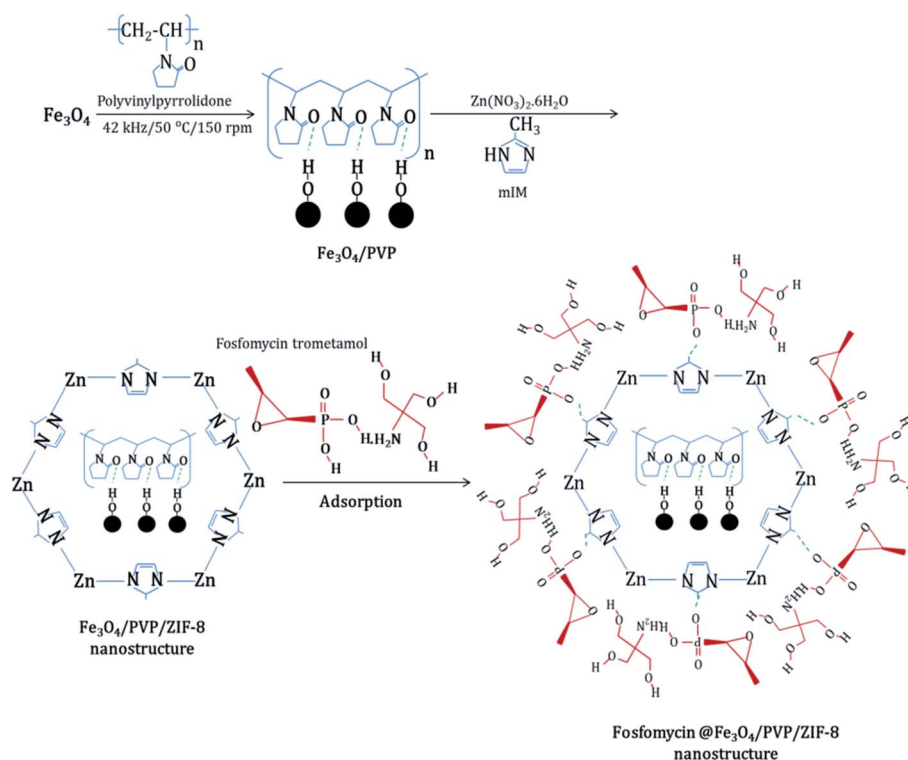

Fig. 1 Schematic diagram for the synthesis of core–shell Fe$_3$O$_4$/PVP/ZIF-8 nanostructure adsorbent and adsorption of Fosfomycin on its surface.

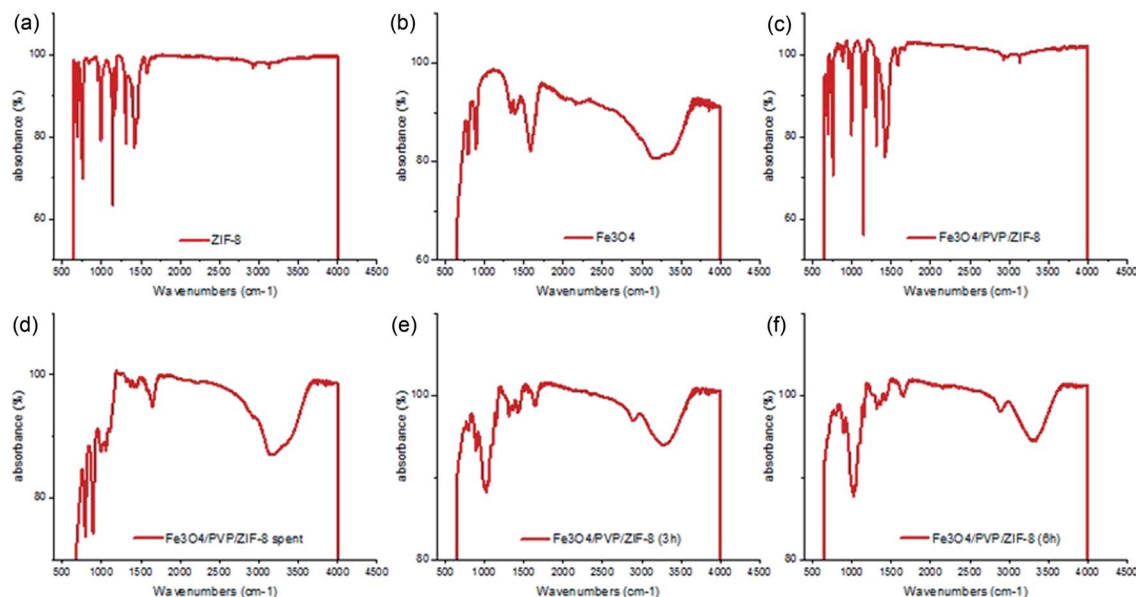**Fig. 2** FTIR spectra of: (a) ZIF-8; (b) Fe_3O_4 nanoparticles; (c) core−shell Fe_3O_4/PVP/ZIF-8 nanostructure; (d) spent core−shell Fe_3O_4/PVP/ZIF-8 nanostructure; (e) core−shell Fe_3O_4/PVP/ZIF-8 nanostructure at pH = 2 for 3 h; (f) core−shell Fe_3O_4/PVP/ZIF-8 nanostructure at pH = 2 for 6 h.

shell Fe_3O_4/PVP/ZIF-8 nanostructure adsorbent was mixed with new successive additions of synthetic Fosfomycin pharmaceutical wastewater.

3   Results and discussion

3.1   Characterization of core–shell Fe_3O_4/PVP/ZIF-8 nanostructure adsorbent

Fig. 2 shows the FTIR spectrums of ZIF-8, magnetite, fresh core–shell Fe_3O_4/PVP/ZIF-8 nanostructure adsorbent, spent core–shell Fe_3O_4/PVP/ZIF-8 nanostructure adsorbent, core–shell Fe_3O_4/PVP/ZIF-8 nanostructure at pH = 2 for 3 h, and core–shell Fe_3O_4/PVP/ZIF-8 nanostructure at pH = 2 for 6 h, respectively. The IR spectrum of ZIF-8 exhibited a weak peak at 3133 cm^{-1} corresponding to the N–H stretching band, while the C–H stretching bands of the methyl groups appeared at 2924 cm^{-1} (imidazole aliphatic C–H) and 1308 cm^{-1}. Besides, the peaks at 1457, 1417, 1179, 1145, and 993 cm^{-1} correspond to C–N and C=N bands and are displaced due to the coordination with the metallic center. Moreover, the C=N band at 1584 cm^{-1} exhibited an axial deformation. The Zn–N stretching recorded absorption bands at 758 and 692 cm^{-1}. These correspond agree with the previous results of ZIF-8 containing the 2-methyl-imidazole ligand that was previously reported in the literature.[46,47]

The FTIR spectrum obtained from magnetite nanoparticles shows two peaks between 650 cm^{-1} and 894 cm^{-1} that are assigned to the stretching vibration modes associated with the metal–oxygen Fe–O bonds in the crystalline lattice of Fe_3O_4. In particular, all spinel structures and ferrites have characteristics of these peaks. The intense band at 1575 cm^{-1} is attributed to OH-bending, and the broadband centered at 3181 cm^{-1} is attributed to OH-stretching. The presence of hydroxyl groups is
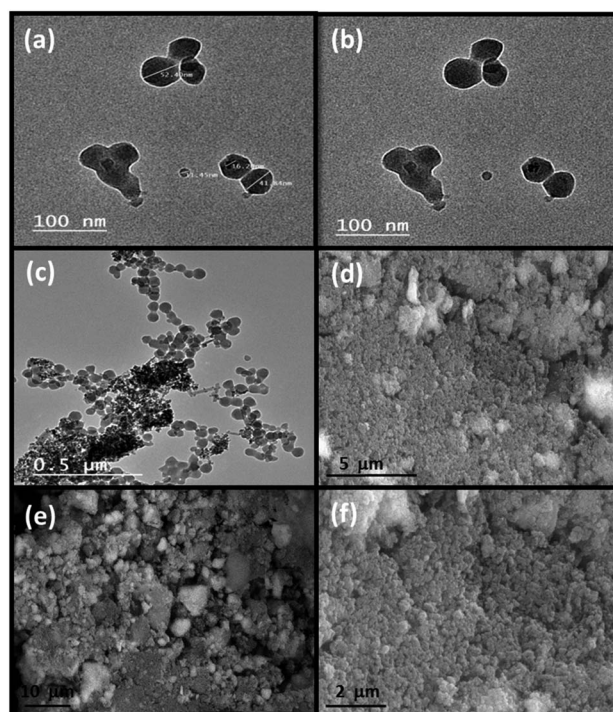
related to the H_2O molecules that may be adsorbed on the Fe_3O_4 surface.

By comparing the FTIR spectrum of core–shell Fe_3O_4/PVP/ZIF-8 nanostructure adsorbent with those of ZIF-8 and Fe_3O_4

Fig. 3 (a−c) TEM images of core−shell Fe_3O_4/PVP/ZIF-8 nanostructure adsorbent at different magnifications demonstrating the successful formation of core−shell structures; (d−f) SEM images of core−shell Fe_3O_4/PVP/ZIF-8 nanostructure adsorbent at different magnifications.

nanoparticles, it was observed that the IR spectrum of core–shell Fe_3O_4/PVP/ZIF-8 nanostructure adsorbent is very similar to the IR spectrum of ZIF-8. In addition, no characteristic peaks for PVP or Fe_3O_4 are observed because of the covering of Fe_3O_4/PVP with layers of the ZIF-8 ligand network. In this case, the Fe_3O_4/PVP acts as the core while the ZIF-8 layers play the role of shell leading to the successful synthesis of core–shell structure.

IR spectrums of the spent core–shell Fe_3O_4/PVP/ZIF-8 nanostructure adsorbent, core–shell Fe_3O_4/PVP/ZIF-8 nanostructure at pH = 2 for 3 h, and core–shell Fe_3O_4/PVP/ZIF-8 nanostructure at pH = 2 for 6 h revealed the presence of the Zn–N stretching vibration mode, which is considered the distinguishing band of ZIF-8. Furthermore, ZIF-8 is characterized by high stability under different conditions, it is stable for an entire year in the ambient atmosphere, for 14 days underwater at ambient pressure, and 24 h underwater at pH = 2.[48]

TEM images of core–shell Fe_3O_4/PVP/ZIF-8 nanostructure adsorbent are shown in Fig. 3(a)–(c). The images show that the Fe_3O_4 nanoparticles lie in the core of the ZIF-8 framework according to the expected construction of the core–shell nanostructure. Besides, the core–shell structures are continuous, uniform, and formed in the nanoscale. Furthermore, the ZIF-8 particles are found in rhombic dodecahedron crystal structures with a smooth surface and a size of less than 100 nm. The thicknesses of the ZIF-8 layers on different Fe_3O_4 vary from one particle to another, as it is very difficult to control the MOF growth on each particle. Similar results were reported in previous studies in the literature.[49,50] However, from Fig. 3(a), it could be observed that the Fe_3O_4 nanoparticles lie in the center (core) of ZIF-8 structures that appeared as distinguishable layers with different sizes. The size of Fe_3O_4 nanoparticles ranged from 11–16 nm, and the ZIF-8 layers with different thicknesses varied from 5 to 20 nm approximately, while the core–shell
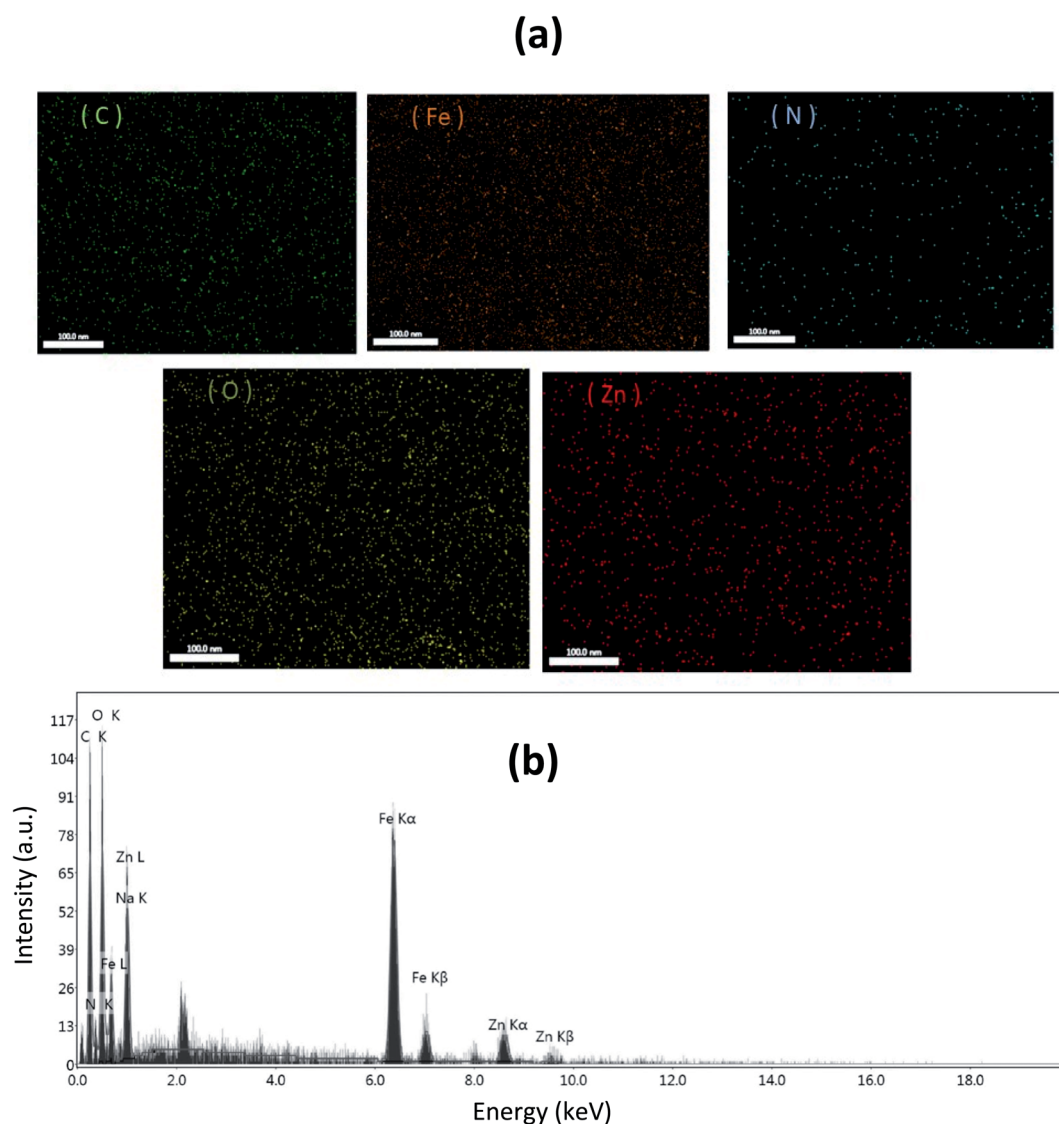

Fig. 4 (a) Energy-dispersive X-ray (EDX) elemental mapping of (C), (Fe), (N), (O), and (Zn); (b) EDX spectrum of core–shell Fe_3O_4/PVP/ZIF-8 nanostructure.

Table 1 Weight% of (C), (N), (O), (Fe), and (Zn) based on EDX mapping of core–shell Fe_3O_4/PVP/ZIF-8 nanostructure adsorbent

Element	Weight %	Atomic%	Net int.	Error%
C K	31.29	48.37	33.9	11.37
N K	9.06	12	4.57	25.52
O K	24.43	28.35	37.47	12.69
Na K	0.01	0.01	0.03	16.23
Fe K	26.1	8.68	76.11	5.21
Zn K	9.11	2.59	12.56	18.15
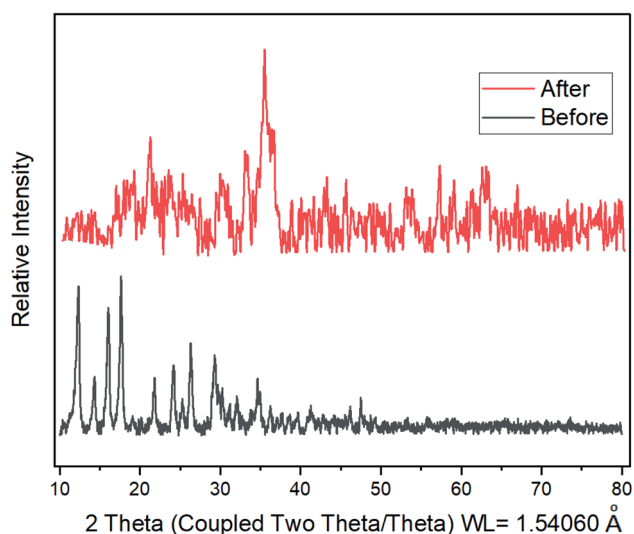
Fig. 5 XRD patterns of core–shell Fe_3O_4/PVP/ZIF-8 nanostructure adsorbent; before Fosfomycin adsorption (lower gray line), after Fosfomycin adsorption at pH 2 for 6 h (upper red line).

Fe_3O_4/PVP/ZIF-8 nanostructure have achieved sizes from 41–52 nm.

SEM images of core–shell Fe_3O_4/PVP/ZIF-8 nanostructure adsorbent are shown in Fig. 3(d)–(f). It could be observed that the ZIF-8 network was successfully loaded onto the surfaces of

all Fe_3O_4 nanoparticles and formed homogenous rough surfaces. These rough surfaces may provide a huge number of cavities and large external surface area for improving the adsorption of adsorbate species.

In Fig. 4 and Table 1, the EDS analysis for the core–shell Fe_3O_4/PVP/ZIF-8 nanostructure adsorbent illustrates that the distribution of Fe and O elements maps have the same symmetry and density with convergent weights% to 26.1 and 24.43, respectively. On the other hand, the elements maps of C, Zn, and N revealed similar symmetry but with lower densities and more spaced distances for particles distributions with a weight% of 31.29 for C and convergent weights% for both Zn, and N to 9.11 and 9.06, respectively. These further supports that the Fe_3O_4 nanoparticles have successfully coated by a network of ZIF-8 layers like a shell. The inter-particles distributions of C, Zn, and N elements are more spacious than that for Fe and O, which further demonstrated that the Fe_3O_4 nanoparticles were surrounded by ZIF-8.

Fig. 5 illustrates the XRD analysis of core–shell Fe_3O_4/PVP/ZIF-8 nanostructure adsorbent before and after adsorption of Fosfomycin antibiotic. It is observed that the core–shell Fe_3O_4/PVP/ZIF-8 nanostructure adsorbent has a good crystallinity with distinguishable sharp peaks referring to ZIF-8 crystals with the presence of characteristic peaks of Fe_3O_4 at $2\theta = 29.77, 35.06,$ and $56.32°$, which correspond to the (220), (311), and (511) crystal facets of the magnetite (COD 9004155). The high stability of core–shell Fe_3O_4/PVP/ZIF-8 nanostructure adsorbent under rigorous adsorption conditions was shown through the XRD pattern done after Fosfomycin adsorption. The changes occurred in the crystallinity of the adsorbent nanostructure and intensities of peaks may be an indication of the formation of different structures due to adsorption of Fosfomycin molecules over the surface and pores of the nanostructure. Previous studies showed similar results for the preparation and properties of magnetically recoverable catalysts by loading Fe_3O_4 nanoparticles inside ZIF-8 compared to the Fe_3O_4 nanoparticles and ZIF-8 framework separately.[51,52]
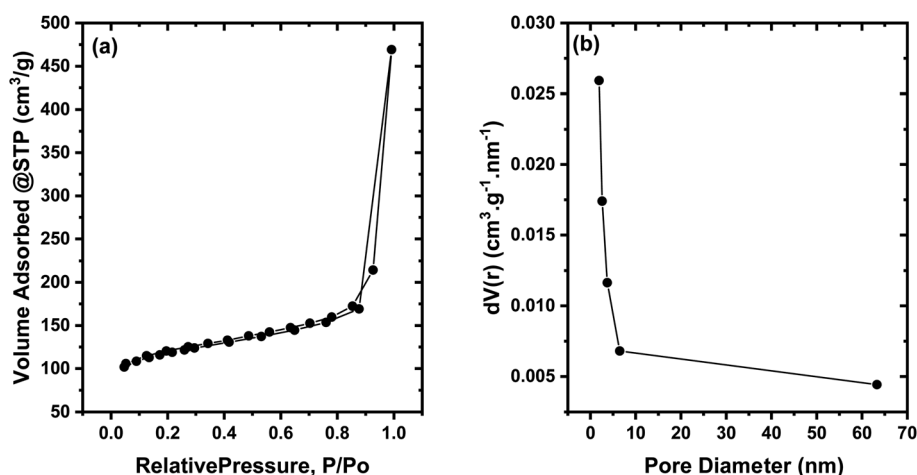
Fig. 6 (a) The N_2 gas adsorption–desorption measurements of core–shell Fe_3O_4/PVP/ZIF-8 nanostructure adsorbent; (b) pore size distribution adsorption as estimated by BJH theory.
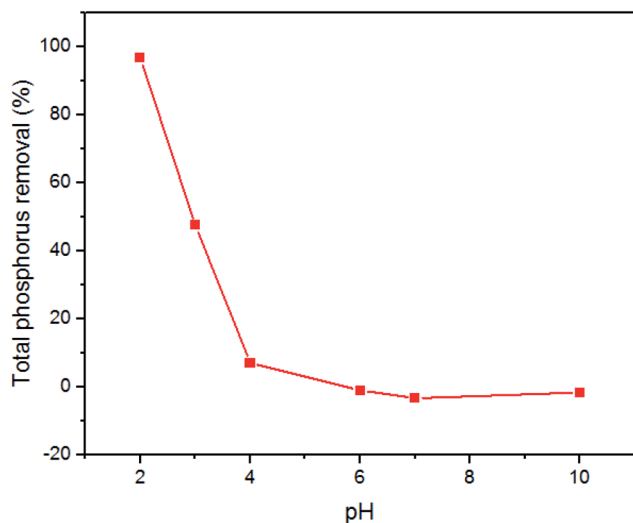
Fig. 7 pH *vs.* % TP removal. Conditions: 0.3 g/100 mL, 30 mg-P L^{-1} initial concentration of TP, 200 rpm, 75 min, and 25 °C.

The BET surface area and pore size distribution of core–shell Fe$_3$O$_4$/PVP/ZIF-8 nanostructure adsorbent were obtained using N$_2$ adsorption–desorption isotherm. As shown in Fig. 6(a), the core–shell Fe$_3$O$_4$/PVP/ZIF-8 nanostructure adsorbent exhibited a type II isotherm. According to the BET method, the BET surface area of core–shell Fe$_3$O$_4$/PVP/ZIF-8 nanostructure adsorbent was calculated as 378.45 m^2 g^{-1}. Furthermore, the core–shell Fe$_3$O$_4$/PVP/ZIF-8 nanostructure adsorbent exhibited

a total pore volume of 0.728 cm^3 g^{-1}. Besides, the pore diameter distribution of core–shell Fe$_3$O$_4$/PVP/ZIF-8 nanostructure adsorbent showed congruent pores with diameters of 1.93 nm resulting in a micro-porous material (<2 nm) (Fig. 6(b)). According to these results, the high surface area and large pore volumes with the micro-porous structure allows the nano-structure to provide more active sites for antibiotic adsorption. Previous studies mentioned similar results.[52,53]

3.2 Effect of pH on the adsorption process

A set of separate batch experiments were performed in a pH range of 2–10 (industrial wastewater's pH range) to evaluate the effect of solution pH on Fosfomycin adsorption onto the surface of core–shell Fe$_3$O$_4$/PVP/ZIF-8 nanostructure adsorbent. The effects of solution pH on the removal percentage of the total phosphorus are shown in Fig. 7. The decrease in the solution pH enhanced the Fosfomycin removal. This can be attributed to the that the ζ-potential of core–shell Fe$_3$O$_4$/PVP/ZIF-8 nano-structure adsorbent becomes more positive in the acidic medium due to protonation of the amino moiety of ZIF-8 surface with the decrease in the solution pH.[54–56]

On the other hand, the Fosfomycin molecules are protonated in the presence of a huge number of H$^+$ ions in the acidic medium, where it changes to a phosphonomycin form (Fig. 8(a)). As a result of the aforementioned conditions, the Fosfomycin adsorption increases at lower pH values due to the higher electrostatic interactions, and the formation of hydrogen bonds between the Fosfomycin molecules and the surface of core–shell Fe$_3$O$_4$/PVP/ZIF-8 nanostructure adsorbent. In
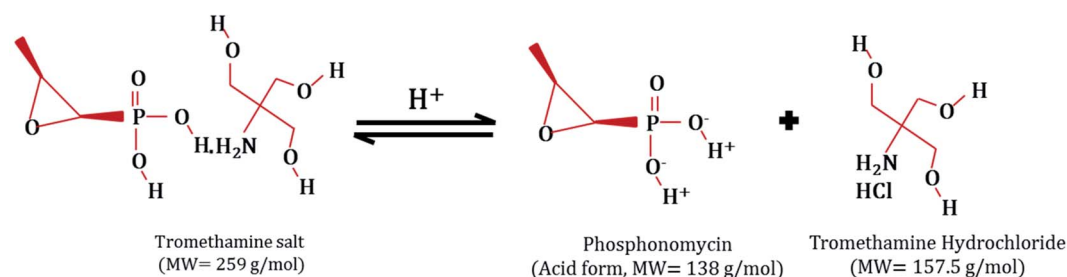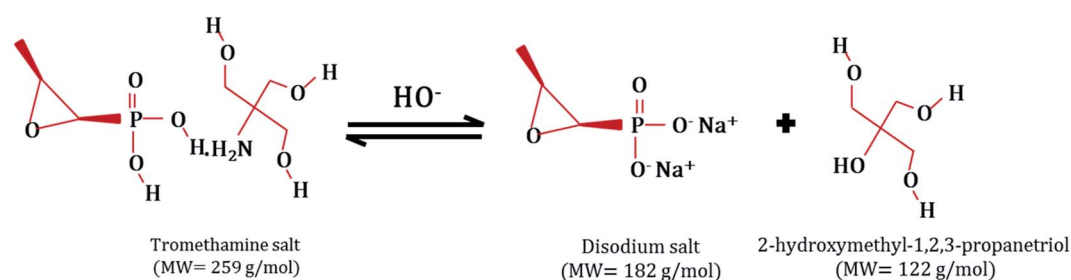

Fig. 8 The Fosfomycin behavior in (a) acidic medium, and (b) alkaline medium.

Table 2 Effect of solution pH on Fosfomycin removal

Conditions	Initial TP concentration	Final concentration
Core–shell Fe_3O_4/PVP/ZIF-8 nanostructure adsorbent dosage = 0.3 g, 200 RPM, 75 min, pH = 2	30 mg-P L^{-1}	0 mg-P L^{-1}
No adsorbent dosage, 200 RPM, 75 min, pH = 2	30 mg-P L	30 mg-P L^{-1}

Table 3 Matrix of coded and uncoded independent variables and the responses of each point

	Dosage (g)		Initial concentration (mg-P L^{-1})		Time (min)		% Removal
Run	Uncoded	Coded	Uncoded	Coded	Uncoded	Coded	R
1	0.1	−1	30	−1	180	1	99.07
2	0.1	−1	30	−1	30	−1	83.4
3	0.1	−1	465	0	105	0	20.65
4	0.1	−1	900	1	30	−1	20.7
5	0.1	−1	900	1	180	1	17.24
6	0.3	0	30	−1	105	0	100
7	0.3	0	465	0	105	0	75.48
8	0.3	0	465	0	105	0	75.48
9	0.3	0	465	0	180	1	60.95
10	0.3	0	465	0	105	0	75.48
11	0.3	0	465	0	30	−1	47.87
12	0.3	0	465	0	105	0	74.75
13	0.3	0	900	1	105	0	33.82
14	0.5	1	30	−1	180	1	100
15	0.5	1	30	−1	30	−1	100
16	0.5	1	465	0	105	0	87.83
17	0.5	1	900	1	30	−1	66.58
18	0.5	1	900	1	180	1	66.58

addition, the hydrophobic and π–π interaction between the oxirane rings of the Fosfomycin and the aromatic imidazole rings of the ZIF-8 should be taken into account. On contrary, in an alkaline medium, the number of hydroxyl ions increases at higher pH. Thus, the Fosfomycin is expected to be in the disodium salt form (Fig. 8(b)). Therefore, the Fosfomycin removal efficiency decreases because of the higher electrostatic repulsion, and instead, the favorable adsorption of HO^- ions increases. Similar behavior was reported in the literature on the adsorption of benzotriazoles on ZIF-8 from aqueous solutions.[57]

To check if the acidic pH value of the Fosfomycin solutions has a significant effect on the removal of the Fosfomycin along with the presence/absence of core–shell Fe_3O_4/PVP/ZIF-8 nanostructure adsorbent, two experiments were done under the same conditions. The first experiment was carried out through the addition of 0.3 g core–shell Fe_3O_4/PVP/ZIF-8 nanostructure adsorbent to Fosfomycin solution with an initial concentration of 30 mg-P L^{-1} as TP. The second experiment was performed without adsorbent dosage addition. The other conditions were maintained constant (solution pH = 2, continuing shaking at 200 rpm for 75 min) for both experiments. It was found that in the absence of core–shell Fe_3O_4/PVP/ZIF-8 nanostructure adsorbent, no Fosfomycin removal occurred. On contrary, the presence of core–shell Fe_3O_4/PVP/

ZIF-8 nanostructure adsorbent resulted in 100% Fosfomycin removal from the aqueous solution as an indication that the core–shell Fe_3O_4/PVP/ZIF-8 nanostructure adsorbent is the
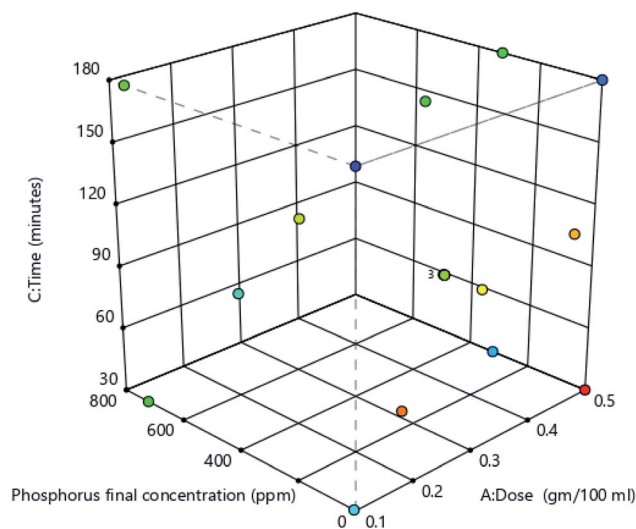

Fig. 9 Graphical representation of the 18 experiments represents the RSM model.

Table 4 The goals of each parameter and response of the 1ˢᵗ optimization model

Name	Goal	Lower limit	Upper limit
A: Dosage	In range	0.1	0.5
B: Phosphorus initial concentration	In range	30	900
C: Time	In range	30	180
% Phosphorus removal	Target = 100	17.2444	100

Table 5 The most desirable solution that was suggested by the model

Number	Dosage (g)	Phosphorus initial concentration (mg-P L^{-1})	Time (min)	Phosphorus final concentration (mg-P L^{-1})	% Phosphorus removal	Desirability
1	0.340	30.225	154.022	5.805	100	1

main reason for the Fosfomycin removal process. Whereas the low pH values of solutions did not contribute to the Fosfomycin removal individually as shown in Table 2.

3.3 The face-centered adsorption model

Central composite design (CCD), the most frequently used technique among RSM designs, was applied to design the experiment (ESI: Table S.1†). RSM is applied to model the effect of the most important operating parameters including dosage of the adsorbent (A), initial concentration of the Fosfomycin as total phosphorus (B), and contact time (C) as mentioned in detail in the ESI (Table S.2†). Table 3 and Fig. 9 show the experimental matrix with the operating conditions of the eighteen runs used to evaluate the effect of independent variables on the % phosphorus removal which is described below in eqn (13) (as a response) as mentioned in detail in the ESI (Table S.3†). This model was fitted linearly with no transformation used as mentioned in the ESI (Table S.4†). The effect of the adsorption time is directly proportional to the % total phosphorus removal. It could be concluded that a contact time of 105 min is sufficient time to reach the equilibrium of Fosfomycin antibiotic molecules adsorption onto the surface of core–shell Fe$_3$O$_4$/PVP/ZIF-8 nanostructure adsorbent. Beyond 105 min of contact time, the amount of Fosfomycin adsorbed on the core–shell Fe$_3$O$_4$/PVP/ZIF-8 nanostructure adsorbent is caused through diffusion through the fluid layer around the adsorbent particle and the pores to the internal adsorption sites. In the initial stages of adsorption of Fosfomycin, the concentration gradient between the layer and the available pore sites is large, and hence, the rate of adsorption is high. Then, the rate of adsorption decreases in the later stages of the adsorption probably due to lowing pore diffusion of the Fosfomycin into the bulk of the adsorbent, which is saturated at about 105 min. The effect of the adsorbent dosage is also directly proportional to the % total phosphorus removal. It could be observed that the lowest dosage of adsorbent has achieved a satisfactory R% which means that the core–shell Fe$_3$O$_4$/PVP/ZIF-8 nanostructure adsorbent possesses a high adsorptive capacity. The decrease in the R% with increasing initial Fosfomycin concentration can be attributed to the fact that at constant adsorbent dosage, the total number of

available adsorption sites present in the core–shell Fe$_3$O$_4$/PVP/ZIF-8 nanostructure adsorbent surface is fixed. While the initial concentration of the pollutant is inversely proportional to the % total phosphorus removal as shown below in Table 3. This implies that a certain amount of core–shell Fe$_3$O$_4$/PVP/ZIF-8 nanostructure adsorbent adsorbs almost the same amount of Fosfomycin antibiotic molecules, resulting in a decrease in the R%. However, the initial concentration of the Fosfomycin molecules provides the necessary driving force to overcome the mass transfer resistance and enhances the interaction between the Fosfomycin antibiotic molecules in the aqueous phase and the core–shell Fe$_3$O$_4$/PVP/ZIF-8 nanostructure adsorbent surface. Therefore, a higher initial concentration of Fosfomycin antibiotic molecules results in an increased rate of adsorption.

$$\% \text{ Removal} = \frac{C_{\text{in}} - C_{\text{out}}}{C_{\text{in}}} \times 100 \tag{13}$$

Two optimization models were performed. The first one is shown in Table 4. The target of the model is to have complete removal of the phosphorus while maintaining the parameters in the design range. This model gives 87 optimum points (ESI: Table S.5†). The first solution, which is the most suggested one, is mentioned below in Table 5.

The 3-D surface responses of phosphorus final concentration, % phosphorus removal, and desirability are shown below in Fig. 10. Regarding the % phosphorus removal surface response, at 0.5 g adsorbent dosage, 30 mg-P L^{-1} initial concentration gave the maximum % phosphorus removal. The 3-D surface response of desirability shows the locus that gives the desirability of 1 which is the optimized locus according to the model goals.

The second model's goal is to minimize the operating conditions (minimize dose and contact time) to give the highest possible removal of the TP under the highest initial TP concentration as shown in Table 6. This model gives 22 optimum solutions (ESI: Table S.6†). The first solution, which is the most suggested one, is mentioned below in Table 7.

The 3-D surface responses of phosphorus final concentration, % phosphorus removal, and desirability are shown below in Fig. 11. Regarding the phosphorus final concentration and %
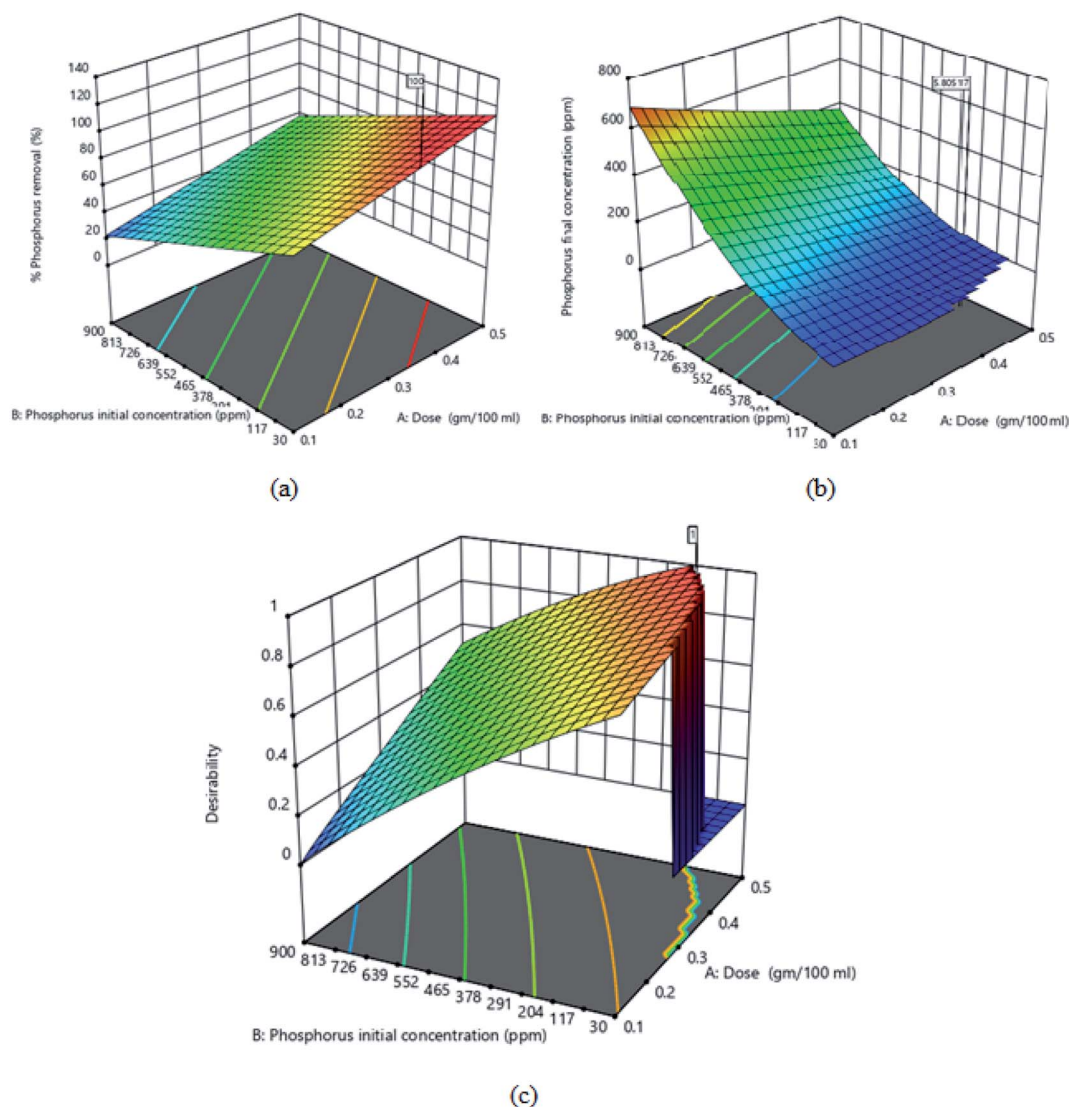
Paper

Fig. 10 First model 3D surface response of (a) % phosphorus removal; (b) phosphorus final conc.; (c) desirability.

Table 6 The goals of each parameter and response of the 2nd optimization model

Name	Goal	Lower limit	Upper limit
A: Dosage	Minimize	0.1	0.5
B: Phosphorus initial concentration	Maximize	30	900
C: Time	Minimize	30	180
% Phosphorus removal	Target = 100	17.2444	100

Table 7 The most desirable solution that was suggested by the model

Number	Dosage (g)	Phosphorus initial concentration (mg-P L^{-1})	Time (min)	Phosphorus final concentration (mg-P L^{-1})	% Phosphorus removal	Desirability
1	0.100	327.845	30.000	153.089	55.225	0.650

phosphorus removal surface responses, at 0.5 g adsorbent dosage, 30 mg-P L^{-1} initial concentration gave the minimum phosphorus final concentration and maximum % phosphorus removal. The 3-D surface response of desirability shows the locus that gives the desirability of 0.65, which is the optimized locus according to the model goals.
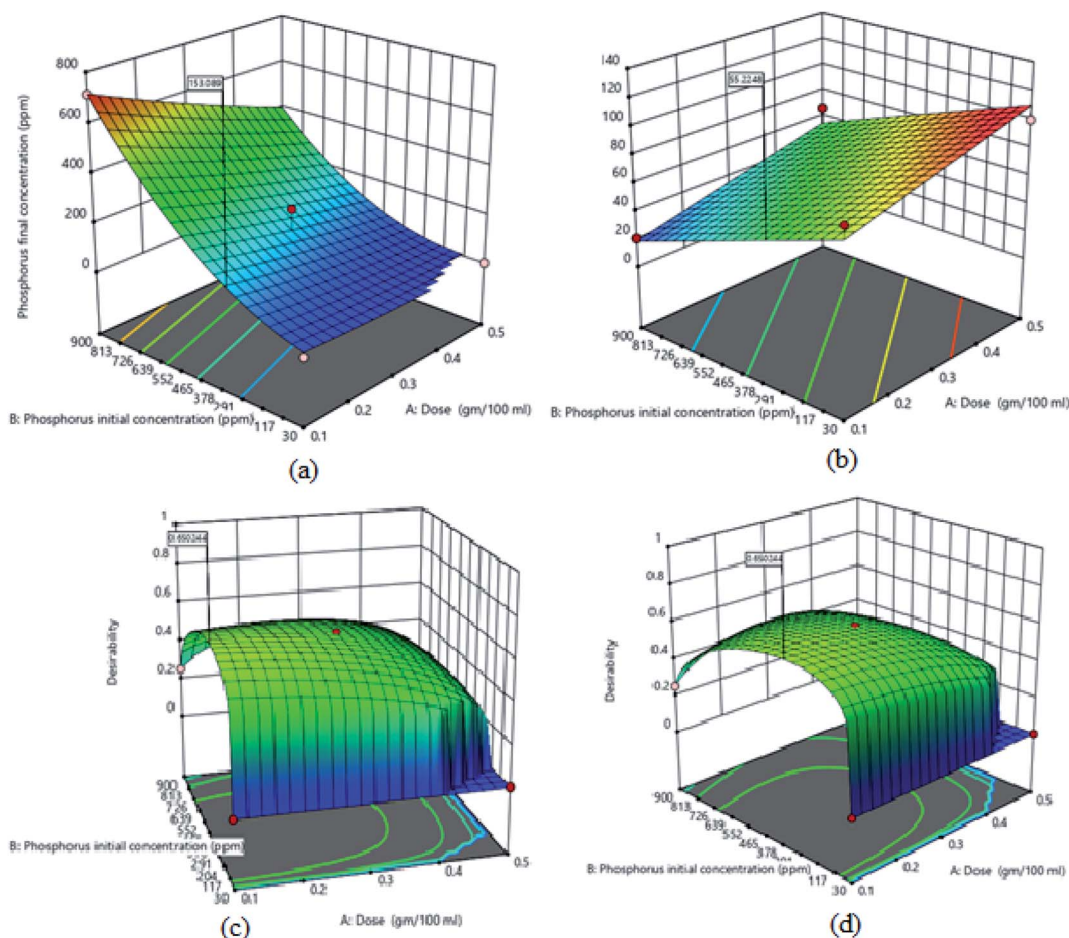
Fig. 11 Second model 3D surface response of (a) phosphorus final conc.; (b) % phosphorus removal; (c) and (d) desirability.

Table 8 Summary of the accuracy of the % phosphorus removal prediction equation

Std. dev.	13.47	R^2	0.8124
Mean	66.99	Adjusted R^2	0.7722
C.V.%	20.11	Predicted R^2	0.6649
		Adeq precision	15.2009

3.4 Coded, actual equations, and validation

3.4.1 Final equation in terms of coded factors. The equation in terms of coded factors can be used to make predictions about the response for given levels of each factor. By default, the high levels of the factors are coded as +1 and the low levels are coded as −1. The coded equation is useful for identifying the relative impact of the factors by comparing the factor coefficients. Current, recommended transform: % phosphorus removal is none.

$$\% \text{ Phosphorus removal} = +66.99 + 17.99A - 27.75B + 2.53C$$

3.4.2 Final equation in terms of actual factors. The equation in terms of actual factors can be used to make predictions

Table 9 Summary of ANOVA test

Source	Sum of squares	D_f	Mean square	F-Value	p-Value	
Model	11 003.41	3	3667.80	20.21	<0.0001	Significant
A – dosage	3237.06	1	3237.06	17.83	0.0009	
B – phosphorus initial concentration	7702.48	1	7702.48	42.43	<0.0001	
C – time	63.88	1	63.88	0.3519	0.5625	
Residual	2541.33	14	181.52			
Lack of fit	2540.93	11	230.99	1733.86	<0.0001	Significant
Pure error	0.3997	3	0.1332			
Cor total	13 544.75	17				

Table 10 A detailed analysis of the model

| Run order	Actual value	Predicted value	Residual	Leverage	Internally studentized residuals	Externally studentized residuals	Cook's distance	Influence on fitted value DFFITS	Standard order
1	75.48	66.99	8.49	0.056	0.648	0.634	0.006	0.154	17
2	99.07	79.28	19.78	0.356	1.829	2.021	0.462	1.501	5
3	100.00	115.27	−15.27	0.356	−1.411	−1.469	0.275	−1.091	6
4	66.58	54.70	11.88	0.356	1.098	1.107	0.166	0.822	4
5	83.40	74.23	9.17	0.356	0.848	0.839	0.099	0.623	1
6	20.65	49.00	−28.36	0.156	−2.290	−2.791	0.242	−1.198	9
7	75.48	66.99	8.49	0.056	0.648	0.634	0.006	0.154	15
8	66.58	59.76	6.82	0.356	0.630	0.616	0.055	0.458	8
9	20.71	18.72	1.99	0.356	0.184	0.178	0.005	0.132	3
10	60.95	69.52	−8.57	0.156	−0.693	−0.679	0.022	−0.291	14
11	17.24	23.78	−6.53	0.356	−0.604	−0.590	0.050	−0.438	7
12	75.48	66.99	8.49	0.056	0.648	0.634	0.006	0.154	18
13	33.82	39.24	−5.42	0.156	−0.438	−0.425	0.009	−0.182	12
14	100.00	94.75	5.25	0.156	0.424	0.412	0.008	0.177	11
15	87.83	84.99	2.84	0.156	0.230	0.222	0.002	0.095	10
16	47.87	64.47	−16.60	0.156	−1.340	−1.384	0.083	−0.594	13
17	74.75	66.99	7.76	0.056	0.592	0.578	0.005	0.140	16
18	100.00	110.21	−10.21	0.356	−0.944	−0.940	0.123	−0.698	2
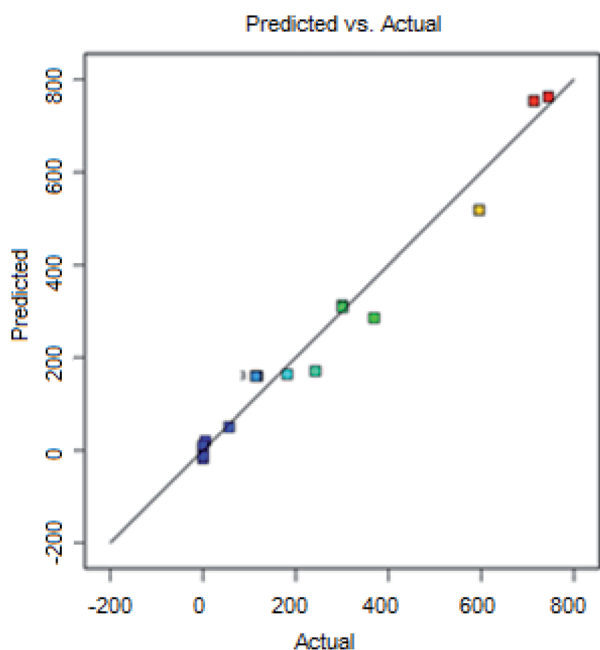
Fig. 12 Predicted *vs.* actual.

about the response for given levels of each factor. Here, the levels should be specified in the original units for each factor. This equation should not be used to determine the relative impact of each factor because the coefficients are scaled to accommodate the units of each factor and the intercept is not at the center of the design space.

$$\% \text{ Phosphorus removal} = +66.13454 + 89.95918 \times \text{dosage} - 0.063801 \times \text{phosphorus initial concentration} + 0.033699 \times \text{time}$$

The predicted R^2 of 0.6649 is in reasonable agreement with the adjusted R^2 of 0.7722; *i.e.* the difference is less than 0.2. Adeq precision measures the signal-to-noise ratio. A ratio greater than 4 is desirable. The ratio of 15.201 indicates an adequate signal as shown in Table 8. This model can be used to navigate the design space.

The model *F*-value of 20.21 implies that the model is significant. There is only a 0.01% chance that an *F*-value this large could occur due to noise. *p*-Values less than 0.0500 indicate model terms are significant. In this case, *A*, and *B* are significant model terms. Values greater than 0.1000 indicate that the model terms are not significant. If there are many

Table 11 Validation of both models inside the design range

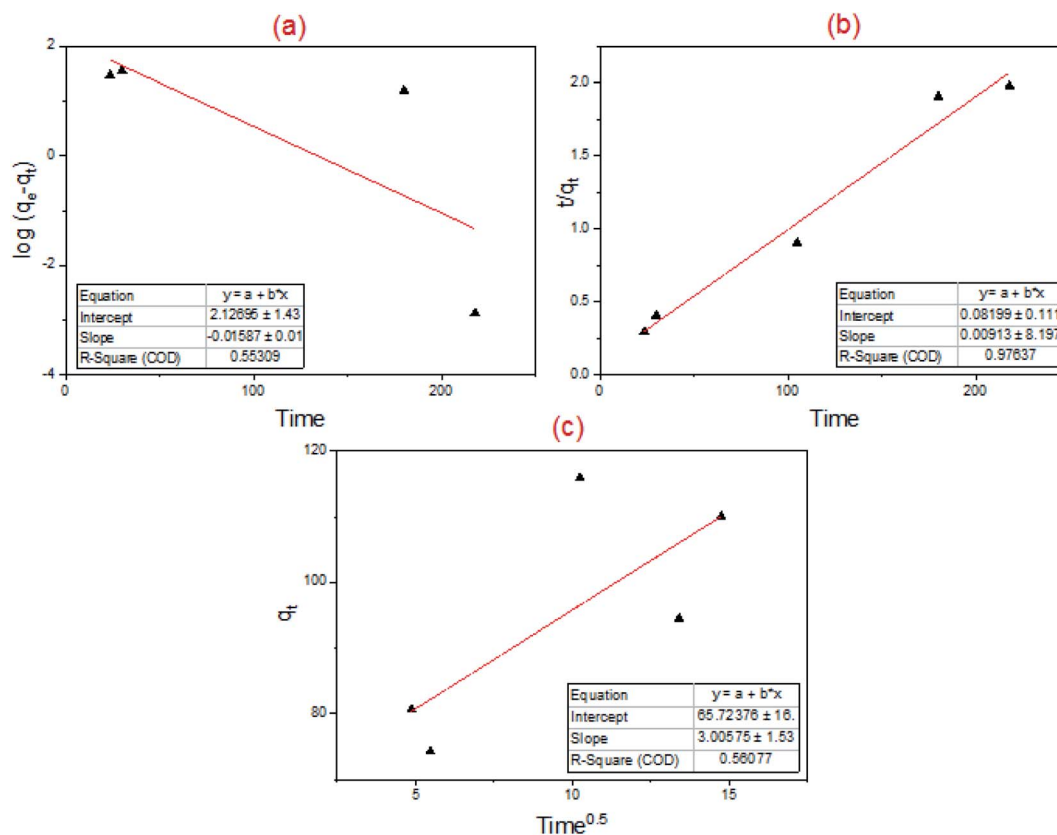| Dosage (g)	Phosphorus initial concentration (mg-P L^{-1})	Time (min)	Phosphorus final concentration (predicted) (mg-P L^{-1})	% Phosphorus removal (predicted)	Phosphorus final concentration (actual) (mg-P L^{-1})	% Phosphorus removal (actual)	% Phosphorus removal rrror
0.5	465	142.3	70.23	86.24	77.6	83.31	4%
0.1	900	30	710.16	18.72	713.60	20.71	10%
0.5	900	180	370.66	59.76	300.80	66.58	10%
0.3	465	105	142.01	66.99	114.00	75.48	11%
0.3	30	105	0.78	94.75	0	100	5%

Fig. 13 Kinetics models: (a) pseudo 1st order model; (b) pseudo 2nd order model; (c) intra–particle diffusion kinetic model.

Table 12 Values of constants and R^2 of each model

Pseudo-first-order		Pseudo-second-order		Intra-particle diffusion kinetic model	
K_1 (min^{-1})	0.0364	K_2 (g mg^{-1} min^{-1})	0.001	K_p (mg g^{-1} min$^{-0.5}$)	3.0058
q_e (mmol g^{-1})	105.73	q_e (mmol g^{-1})	109.89		
R^2	0.5438	R^2	0.9764	R^2	0.5608

insignificant model terms (not counting those required to support hierarchy), model reduction may improve your model. The lack of fit F-value of 1733.86 implies the lack of fit is significant. There is only a 0.01% chance that a lack of fit F-value this large could occur due to noise as shown in Table 9 below. A detailed analysis report is shown in Table 10 and Fig. 12, which validates the model.

3.5 Validation check

The accuracy of the model was checked as shown in Table 11 and the errors are considerably small.

3.6 Kinetics

Optimum operating conditions can be selected by kinetics studies on batch adsorption systems. In the present work, the experimental data were fitted to three of the most widely used kinetic models as shown in Fig. 13. Table 12 shows the fitted experimental data with the pseudo-first-order, pseudo-second-

order, and intra-particle diffusion kinetic model. As seen, the pseudo-second-order kinetic model with higher R^2 values showed better compliance with the experimental data, suggesting that chemisorption is the adsorption-determining step.

3.7 Isotherms

Phosphorus adsorption (Fosfomycin) onto the surface of core–shell Fe_3O_4/PVP/ZIF-8 nanostructure adsorbent was described by Langmuir, Freundlich, Temkin, and Dubinin–Radushkevich isotherm models. Fig. 14 and Table 13 summarize the results. Monolayer surface coverage was assumed by the Langmuir model *versus* multilayer adsorption on a heterogeneous surface that was assumed by the Freundlich model. From the linearized fitting, the Freundlich isotherm equation ($R^2 = 0.9505$) has described the system better than the Langmuir isotherm equation ($R^2 = 0.8712$), Temkin isotherm equation ($R^2 = 0.833$), and Dubinin–Radushkevich isotherm equation ($R^2 = 0.16563$). The *n*-value of the Freundlich isotherm lies between 1 and 10, which is a good indicator of favorable adsorption.[58]
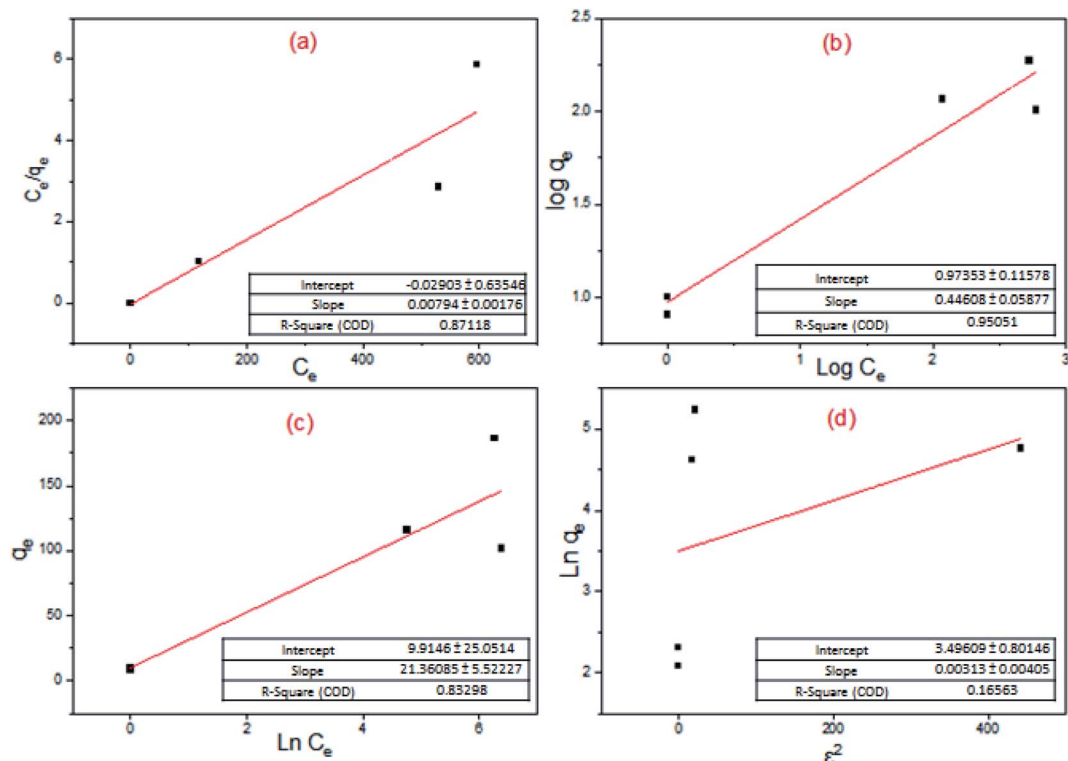
Fig. 14 Adsorption isotherms: (a) Langmuir isotherm; (b) Freundlich isotherm; (c) Temkin isotherm; (d) Dubinin–Radushkevich isotherm.

Table 13 Values of constants and R^2 of each model

Langmuir isotherm		Freundlich isotherm		Temkin isotherm		Dubinin–Radushkevich isotherm	
Q_m (mg g^{-1})	126.58	n_F (g L^{-1})	2.242	k_t (L mg^{-1})	1.591	q_m (mg g^{-1})	32.987
K_L (L mg^{-1})	0.272	K_F (mg g^{-1})	9.408	B_1	21.361	β (mol^2 J^{-2})	0.0031
R^2	0.8712	R^2	0.9505	R^2	0.833	R^2	0.1656

Table 14 Values of R_L at each initial concentration

Initial conc.	R_L
24	0.132837407
30	0.109170306
465	0.007844368
900	0.004068348
1090	0.003361571

Furthermore, the value of $1/n$, which was obtained from the slope of the linear plot of $\log(q_e)$ *vs.* $\log(C_e)$ of the Freundlich isotherm, was below unity implying that chemisorption is the governing process.[59] The separation factor, R_L as obtained from the Langmuir isotherm model was lower than unity, which likewise indicating to a favorable adsorption process as shown in Table 14.[60]

3.8 Stability

The best adsorbents are highly stable and kinetically favorable under frequent adsorption conditions. Some adsorbents,
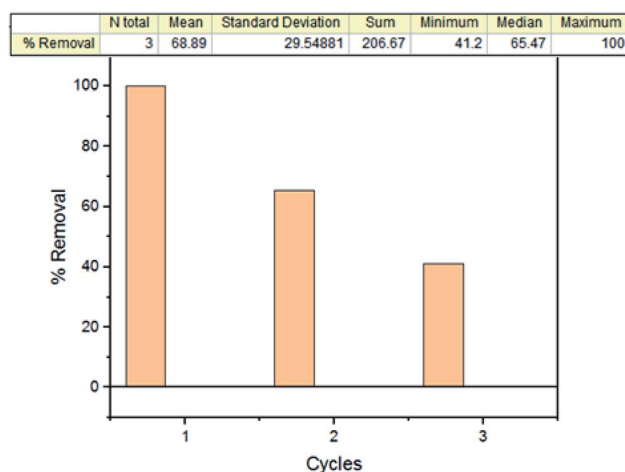

	N total	Mean	Standard Deviation	Sum	Minimum	Median	Maximum
% Removal	3	68.89	29.54881	206.67	41.2	65.47	100

Fig. 15 % (TP) removal for 0.3 g dosage, 30 mg-P L^{-1} initial concentration, pH = 2, and time of 105 minutes for each cycle.

Table 15 Regeneration results of core–shell Fe_3O_4/PVP/ZIF-8 nanostructure adsorbent for Fosfomycin removal

Dosage (g/100 mL)	Initial conc. (mg-P L^{-1})	Time (min)	% Removal of the new adsorbent	% Removal after regeneration
0.3	465	30	47.87	5.85
0.3	900	105	33.82	15.28

Table 16 Different metal–organic framework adsorbents used in phosphorus removal from aqueous solutions

Adsorbent	Adsorbate	Operation conditions	Uptake	Ref.
Core–shell Fe_3O_4/PVP/ZIF-8 nanostructure	Phosphorus from Fosfomycin pharmaceutical wastewater	Time range (30–180 min), adsorbent dosage range (0.1–0.5 g/100 mL), P conc. range (30–900 mg L^{-1}), at room temperature at 250 rpm and pH 2	High maximal adsorption capacity around 1200 mg-P g^{-1}	Current study
Cubic zeolitic imidazolate framework-8	Phosphorus from aqueous solution	Time range (2–60 min), ZIF-8 dosage range (100–1000 g L^{-1}), P conc. range (5–20 mg L^{-1}), at room temperature at 300 rpm and pH 4	The sorption capacity of ZIF-8 for P was 38.22 mg g^{-1}	65
Fe-based metal–organic frameworks (MOFs), MIL-101 and NH_2-MIL-101	Phosphate from aqueous solutions and eutrophic water	The adsorbent dosage from 10 to 60 mg L^{-1}, contact time to 120 min, and the presence of the co-existing ion of other anions including chloride, bromide, nitrate, and sulfate ions	The concentration of phosphates decreases sharply from the initial 0.60 mg L^{-1} to 0.045 and 0.032 mg L^{-1}, respectively, within just 30 min of exposure	66
(ZIF-67)	Phosphorus from aqueous solution	Time range (10–100 min), ZIF-67 dosage range (0.1–1 g L^{-1}), P conc. range (10–50 mg L^{-1}), at room temperature and at pH range (4–12)	Monolayer adsorption capacity of ZIF-67 for PO_4^{3-} around 92.43 mg g^{-1}	43
Trivalent metal-based NH_2-MIL-101 MOFs	Phosphorus from aqueous solution	pH range of 2–12, time to 250 min, ionic strength (the increase in $NaNO_3$ concentration from 0.001 to 1 M in the solution containing 50 mg L^{-1} of phosphate), at room temperature	High maximal adsorption capacity above 79.414 mg-P g^{-1}	67
La@ZIF-8 composite metal–organic frameworks	Phosphorus from aqueous solution	The initial phosphorus concentration (10–70 mg L^{-1}), dosage (0.004–0.02 g), pH (3–10) and contact reaction time to 720 min	Adsorption capacity (147.63 mg g^{-1})	68
UiO-66 metal–organic frameworks with varying functional groups	Phosphorus from aqueous solution	Using UiO-66-NH_2 at a dosage ≥ 13.5 g L^{-1}, at 25 °C and pH 4	UiO-66-NH_2 displayed the highest adsorption capacity (153.9 mg g^{-1})	69
ZIF-8/hydroxylated MWCNT nanocomposites	Phosphorus from aqueous solution	pH (4, 7, 10), temperature (20, 30, 40), initial concentration 1.0 mg L^{-1}, and speed 200 rpm	Maximum phosphate adsorption capacity of 203.0 mg g^{-1}	70

however, work extremely fast at the beginning but decompose after just a few cycles. Thus, to examine the stability of core–shell Fe_3O_4/PVP/ZIF-8 nanostructure adsorbent over frequent experiments under severe acidic conditions, the core–shell Fe_3O_4/PVP/ZIF-8 nanostructure adsorbent underwent 3 concessive cycles of 105 min each by total an entire 315 min. It was found that the core–shell Fe_3O_4/PVP/ZIF-8 nanostructure adsorbent worked well under a very acidic medium although

the successive trials. The obtained results are shown in Fig. 15. Complete phosphorus removal (30 mg-P L^{-1}) was achieved after the first cycle. However, the removal % was decreased to nearly 65% and 40% in the subsequent two cycles, respectively. Thus, it can be recognized that the core–shell Fe$_3$O$_4$/PVP/ZIF-8 nanostructure adsorbent has decent stability and efficacy towards the removal of Fosfomycin antibiotic under repeated harsh conditions within the range of conditions applied.

3.9 Regeneration

Regeneration of two saturated core–shell Fe$_3$O$_4$/PVP/ZIF-8 nanostructure adsorbents was done. As shown in Table 15, there is an inverse relationship between the initial concentration and regeneration ability. It was noticed that there was a large weight loss during the regeneration due to the loss of the adsorbent mass in the reusability experiments, and due to the severe operating conditions (pH = 2) for a long time. During the regeneration process, the adsorbent that was used at 900 mg-P L^{-1} initial concentration for 105 min, lost weight from 0.3 g to 0.015 g and the adsorbent that was used at 465 mg-P L^{-1} initial concentration for 30 min lost weight from 0.3 g to 0.03 g. This may be assigned to the acid causing the significant dissolution of particles' core (magnetite nanoparticles) into ferrous and ferric ions and migration of ions into the solution causing the solution to turn yellow. Additionally, the sharp fall in Fosfomycin removal could attribute to the instability of core–shell Fe$_3$O$_4$/PVP/ZIF-8 nanostructure adsorbent under strongly acidic conditions for a long time. When the pH of the solution was adjusted to around 2, the solution turbidity disappears gradually due to the partial dissolution of core–shell Fe$_3$O$_4$/PVP/ZIF-8 nanostructure adsorbent.[61–64]

3.10 Comparison with other adsorbents

To demonstrate and emphasize the efficiency and novelty of the current core–shell Fe$_3$O$_4$/PVP/ZIF-8 nanostructure adsorbent, a comparison was performed as shown in Table 16 between the current adsorbent and many types of MOFs composites that were categorized as highly efficient adsorbents used for phosphorus removal.[43,64–69] As shown below, the adsorption capacity of core–shell Fe$_3$O$_4$/PVP/ZIF-8 nanostructure adsorbent was around 1200 mg-P g^{-1}, which is extremely higher than other MOFs adsorbents.

As for the effect of coexisting ions on the adsorption of phosphorous, ZIF-8-based adsorbents show good anti-interference adsorption performance for phosphorus removal in the presence of several coexisting ions such as sulfate, chloride, nitrate, and bicarbonate, while the presence of carbonate results in a considerable hindering of the adsorption.[65] This hindering in the presence of carbonates was attributed to the increase occurring in the pH of the solution, which leads to having a more negative surface charge for ZIF-8 and that cause PO$_4^{3-}$ and HPO$_4^{2-}$ static repulsion.[65] Working with low pH actual pharmaceutical wastewater is expected to have minimal anti-interference even in the presence of the carbonate. Future work will be directed to Fosfomycin antibiotic removal from real wastewater that will give better insight into the effect of coexisting ions.

4 Conclusions

The current study focused on the effect of major design parameters on the adsorption of Fosfomycin antibiotic that was measured as phosphorus onto the surface of core–shell Fe$_3$O$_4$/PVP/ZIF-8 nanostructure adsorbent. Accordingly, the following major conclusions can be drawn:

● When core–shell Fe$_3$O$_4$/PVP/ZIF-8 nanostructure adsorbent is used for Fosfomycin antibiotic (in form of TP) removal from aqueous solutions, design parameters such as initial Fosfomycin (as TP) concentration, initial solution pH, adsorbent dose, and contact time must be studied to detect the optimum conditions that should give the highest (TP) removal%. The adsorption of Fosfomycin (as TP) onto the adsorbent increased markedly at a pH value of 2, which is the actual pH value of most industrial effluents.[42]

● The central composite design (CCD) was found to be an appropriate approach to optimize the variables affecting Fosfomycin (as TP) adsorption. The obtained linear regression model well depicted observed values of percent Fosfomycin (as TP) removal and Fosfomycin (as TP) final concentration.

● The adsorption capacity of core–shell Fe$_3$O$_4$/PVP/ZIF-8 nanostructure adsorbent was around 1200 mg-P g^{-1}, which is significantly higher than other MOFs adsorbents reported in the literature.

● The adsorption kinetics for Fosfomycin (as TP) removal could be well described by the pseudo-second-order equation with a correlation value of $R^2 = 0.9764$, which revealed that chemisorption was the dominant process.

● The adsorption isotherm for Fosfomycin (as TP) removal could be well described by the Freundlich equation with a correlation value of $R^2 = 0.9505$ which revealed that adsorption occurs on a heterogeneous surface through multilayer adsorption.

It is concluded that core–shell Fe$_3$O$_4$/PVP/ZIF-8 nanostructure could be employed as a highly efficient adsorbent for the removal of Fosfomycin antibiotic molecules from aqueous solutions.

Conflicts of interest

There are no conflicts to declare.

References

1 M. Y. D. Alazaiza, A. Albahnasawi, G. A. M. Ali, M. J. K. Bashir, D. E. Nassani, T. Al Maskari, S. S. Abu Amr and M. S. S. Abujazar, Application of Natural Coagulants for Pharmaceutical Removal from Water and Wastewater: A Review, *Water*, 2022, **14**, 1–16, DOI: **10.3390/w14020140**.

2 T. E. Doll and F. H. Frimmel, Fate of pharmaceuticals - Photodegradation by simulated solar UV-light, *Chemosphere*, 2003, **52**, 1757–1769, DOI: **10.1016/S0045-6535(03)00446-6**.

3   M. O. Buffle, J. Schumacher, E. Salhi, M. Jekel and U. von Gunten, Measurement of the initial phase of ozone decomposition in water and wastewater by means of a continuous quench-flow system: Application to disinfection and pharmaceutical oxidation, *Water Res.*, 2006, **40**, 1884–1894, DOI: **10.1016/j.watres.2006.02.026**.

4   L. A. Pérez-Estrada, S. Malato, W. Gernjak, A. Agüera, E. M. Thurman, I. Ferrer and A. R. Fernández-Alba, Photo-fenton degradation of diclofenac: Identification of main intermediates and degradation pathway, *Environ. Sci. Technol.*, 2005, **39**, 8300–8306, DOI: **10.1021/es050794n**.

5   J. Lee, O. K. Farha, J. Roberts, K. A. Scheidt, S. T. Nguyen and J. T. Hupp, Metal-organic framework materials as catalysts, *Chem. Soc. Rev.*, 2009, **38**, 1450–1459, DOI: **10.1039/b807080f**.

6   S. K. Khetan and T. J. Collins, Human pharmaceuticals in the aquatic environment: A challenge to green chemistry, *Chem. Rev.*, 2007, **107**, 2319–2364, DOI: **10.1021/cr020441w**.

7   S. Z. Ahammad, J. Gomes and T. R. Sreekrishnan, Wastewater treatment for production of H_2S-free biogas, *J. Chem. Technol. Biotechnol.*, 2008, **83**, 1163–1169, DOI: **10.1002/jctb**.

8   H. I. Abdel-Shafy and M. S. Mohamed-Mansour, Issue of pharmaceutical compounds in water and wastewater: Sources, impact and elimination, Egypt, *J. Chem.*, 2013, **56**, 449–471, DOI: **10.21608/ejchem.2013.1123**.

9   B. K. Biswas, K. Inoue, K. N. Ghimire, H. Harada, K. Ohto and H. Kawakita, Removal and recovery of phosphorus from water by means of adsorption onto orange waste gel loaded with zirconium, *Bioresour. Technol.*, 2008, **99**, 8685–8690, DOI: **10.1016/j.biortech.2008.04.015**.

10 S. S. Mithra, S. T. Ramesh, R. Gandhimathi and P. V. Nidheesh, Studies on the removal of phosphate from water by electrocoagulation with aluminium plate electrodes, *Environ. Eng. Manage. J.*, 2017, **16**, 2293–2302, DOI: **10.30638/eemj.2017.237**.

11 S. Sengupta and A. Pandit, Selective removal of phosphorus from wastewater combined with its recovery as a solid-phase fertilizer, *Water Res.*, 2011, **45**, 3318–3330, DOI: **10.1016/j.watres.2011.03.044**.

12 G. Qiu, Y. Song, P. Zeng, S. Xiao and L. Duan, Phosphorus recovery from fosfomycin pharmaceutical wastewater by wet air oxidation and phosphate crystallization, *Chemosphere*, 2011, **84**, 241–246, DOI: **10.1016/j.chemosphere.2011.04.011**.

13 A. Hamdy, M. K. Mostafa and M. Nasr, Zero-valent iron nanoparticles for methylene blue removal from aqueous solutions and textile wastewater treatment, with cost estimation, *Water Sci. Technol.*, 2018, **78**, 367–378, DOI: **10.2166/wst.2018.306**.

14 A. S. Mahmoud, M. K. Mostafa and M. Nasr, Regression model, artificial intelligence, and cost estimation for phosphate adsorption using encapsulated nanoscale zero-valent iron, *Sep. Sci. Technol.*, 2019, **54**, 13–26, DOI: **10.1080/01496395.2018.1504799**.

15 A. Hamdy, S. H. Ismail, A. A. Ebnalwaled and G. G. Mohamed, Characterization of Superparamagnetic/Monodisperse PEG-Coated Magnetite Nanoparticles

Sonochemically Prepared from the Hematite Ore for Cd(II) Removal from Aqueous Solutions, *J. Inorg. Organomet. Polym. Mater.*, 2021, **31**, 397–414, DOI: **10.1007/s10904-020-01741-0**.

16 A. Hamdy, Experimental Study of the Relationship Between Dissolved Iron, Turbidity, and Removal of Cu(II) Ion From Aqueous Solutions Using Zero-Valent Iron Nanoparticles, *Arabian J. Sci. Eng.*, 2021, **46**, 5543–5565, DOI: **10.1007/s13369-020-05079-0**.

17 A. Hamdy, M. K. Mostafa and M. Nasr, Techno-economic estimation of electroplating wastewater treatment using zero-valent iron nanoparticles: batch optimization, continuous feed, and scaling up studies, *Environ. Sci. Pollut. Res.*, 2019, **26**, 25372–25385, DOI: **10.1007/s11356-019-05850-3**.

18 A. Hamdy, M. K. Mostafa and M. Nasr, Regression analysis and artificial intelligence for removal of methylene blue from aqueous solutions using nanoscale zero-valent iron, *Int. J. Environ. Sci. Technol.*, 2019, **16**, 357–372, DOI: **10.1007/s13762-018-1677-z**.

19 A. H. Khan, N. A. Khan, M. Zubair, M. Azfar Shaida, M. S. Manzar, A. Abutaleb, M. Naushad and J. Iqbal, Sustainable green nanoadsorbents for remediation of pharmaceuticals from water and wastewater: A critical review, *Environ. Res.*, 2022, **204**, 112243, DOI: **10.1016/j.envres.2021.112243**.

20 B. Boruah, P. K. Samantaray, G. Madras, J. M. Modak and S. Bose, Sustainable photocatalytic water remediation *via* dual active strongly coupled $AgBiO_3$ on PVDF/PBSA membranes, *Chem. Eng. J.*, 2020, **394**, 124777, DOI: **10.1016/j.cej.2020.124777**.

21 E. Barea, C. Montoro and J. A. R. Navarro, Toxic gas removal-metal-organic frameworks for the capture and degradation of toxic gases and vapours, *Chem. Soc. Rev.*, 2014, **43**, 5419–5430, DOI: **10.1039/c3cs60475f**.

22 X. Liu, Y. Zhou, J. Zhang, L. Tang, L. Luo and G. Zeng, Iron Containing Metal-Organic Frameworks: Structure, Synthesis, and Applications in Environmental Remediation, *ACS Appl. Mater. Interfaces*, 2017, **9**, 20255–20275, DOI: **10.1021/acsami.7b02563**.

23 Z. Chen, K. O. Kirlikovali, K. B. Idrees, M. C. Wasson and O. K. Farha, Porous materials for hydrogen storage, *Chem*, 2022, **8**, 693–716, DOI: **10.1016/j.chempr.2022.01.012**.

24 B. Cui and G. Fu, Process of metal–organic framework (MOF)/covalent–organic framework (COF) hybrids-based derivatives and their applications on energy transfer and storage, *Nanoscale*, 2022, **14**, 1679–1699, DOI: **10.1039/D1NR07614K**.

25 Z. Chang, D. H. Yang, J. Xu, T. L. Hu and X. H. Bu, Flexible metal-organic frameworks: Recent advances and potential applications, *Adv. Mater.*, 2015, **27**, 5432–5441, DOI: **10.1002/adma.201501523**.

26 Y. Chen, B. Li, L. Ye and Y. Peng, The combined effects of COD/N ratio and nitrate recycling ratio on nitrogen and phosphorus removal in anaerobic/anoxic/aerobic (A2/O)-biological aerated filter (BAF) systems, *Biochem. Eng. J.*, 2015, **93**, 235–242, DOI: **10.1016/j.bej.2014.10.005**.

27 F. Ahmadijokani, S. Tajahmadi, A. Bahi, H. Molavi, M. Rezakazemi, F. Ko, T. M. Aminabhavi and M. Arjmand, Ethylenediamine-functionalized Zr-based MOF for efficient removal of heavy metal ions from water, *Chemosphere*, 2021, **264**, 128466, DOI: **10.1016/j.chemosphere.2020.128466**.

28 M. Guo, M. Zhang, R. Liu, X. Zhang and G. Li, State-of-the-Art Advancements in Photocatalytic Hydrogenation: Reaction Mechanism and Recent Progress in Metal-Organic Framework (MOF)-Based Catalysts, *Adv. Sci.*, 2022, **9**, 1–28, DOI: **10.1002/advs.202103361**.

29 M. Serhan, M. Sprowls, D. Jackemeyer, M. Long, I. D. Perez, W. Maret, N. Tao and E. Forzani, *Total iron measurement in human serum with a smartphone, AIChE Annual Meeting, Conference Proceedings*, Nov 2019.

30 P. K. Samantaray, G. Madras and S. Bose, Water Remediation Aided by a Graphene-Oxide-Anchored Metal Organic Framework through Pore- and Charge-Based Sieving of Ions, *ACS Sustainable Chem. Eng.*, 2019, **7**, 1580–1590, DOI: **10.1021/acssuschemeng.8b05354**.

31 D. Huang, G. Zhang, J. Yi, M. Cheng, C. Lai, P. Xu, C. Zhang, Y. Liu, C. Zhou, W. Xue, R. Wang, Z. Li and S. Chen, Progress and challenges of metal-organic frameworks-based materials for SR-AOPs applications in water treatment, *Chemosphere*, 2021, **263**, 127672, DOI: **10.1016/j.chemosphere.2020.127672**.

32 C. Tian, J. Zhao, X. Ou, J. Wan, Y. Cai, Z. Lin, Z. Dang and B. Xing, Enhanced Adsorption of p -Arsanilic Acid from Water by Amine-Modified UiO-67 as Examined Using Extended X-ray Absorption Fine Structure, X-ray Photoelectron Spectroscopy, and Density Functional Theory Calculations, *Environ. Sci. Technol.*, 2018, **52**, 3466–3475, DOI: **10.1021/acs.est.7b05761**.

33 P. Kumar, A. Pournara, K. H. Kim, V. Bansal, S. Rapti and M. J. Manos, Metal-organic frameworks: Challenges and opportunities for ion-exchange/sorption applications, *Prog. Mater. Sci.*, 2017, **86**, 25–74, DOI: **10.1016/j.pmatsci.2017.01.002**.

34 Y. Zheng, F. Chu, B. Zhang, J. Yan and Y. Chen, Ultrahigh adsorption capacities of carbon tetrachloride on MIL-101 and MIL-101/graphene oxide composites, *Microporous Mesoporous Mater.*, 2018, **263**, 71–76, DOI: **10.1016/j.micromeso.2017.12.007**.

35 J. Abdi, M. Vossoughi, N. M. Mahmoodi and I. Alemzadeh, Synthesis of metal-organic framework hybrid nanocomposites based on GO and CNT with high adsorption capacity for dye removal, *Chem. Eng. J.*, 2017, **326**, 1145–1158, DOI: **10.1016/j.cej.2017.06.054**.

36 B. Szczęśniak, J. Choma and M. Jaroniec, Gas adsorption properties of hybrid graphene-MOF materials, *J. Colloid Interface Sci.*, 2018, **514**, 801–813, DOI: **10.1016/j.jcis.2017.11.049**.

37 M. O. Abdelmigeed, E. G. Al-Sakkari, M. S. Hefney, F. M. Ismail, A. Abdelghany, T. S. Ahmed and I. M. Ismail, Magnetized ZIF-8 impregnated with sodium hydroxide as a heterogeneous catalyst for high-quality biodiesel

38 M. O. Abdelmigeed, E. G. Al-Sakkari, M. S. Hefney, F. M. Ismail, T. S. Ahmed and I. M. Ismail, Biodiesel production catalyzed by NaOH/Magnetized ZIF-8: Yield improvement using methanolysis and catalyst reusability enhancement, *Renewable Energy*, 2021, **174**, 253–261, DOI: **10.1016/j.renene.2021.04.057**.

39 L. Chen, Y. Peng, H. Wang, Z. Gu and C. Duan, Synthesis of Au@ZIF-8 single- or multi-core-shell structures for photocatalysis, *Chem. Commun.*, 2014, **50**, 8651–8654, DOI: **10.1039/c4cc02818j**.

40 F. W. Gilcreas, Future of standard methods for the examination of water and wastewater, *Health Lab. Sci.*, 1967, **4**(3), 137–141.

41 A. I. Khuri and S. Mukhopadhyay, Response surface methodology, *Wiley Interdiscip. Rev.: Comput. Stat.*, 2010, **2**, 128–149, DOI: **10.1002/wics.73**.

42 D. T. Mekonnen, E. Alemayehu and B. Lennartz, Removal of phosphate ions from aqueous solutions by adsorption onto leftover coal, *Water*, 2020, **12**, 1–15, DOI: **10.3390/W12051381**.

43 S. Mazloomi, M. Yousefi, H. Nourmoradi and M. Shams, Evaluation of phosphate removal from aqueous solution using metal organic framework; Isotherm, kinetic and thermodynamic study, *J. Environ. Health Sci. Eng.*, 2019, **17**, 209–218, DOI: **10.1007/s40201-019-00341-6**.

44 E. N. Peleka and E. A. Deliyanni, Adsorptive removal of phosphates from aqueous solutions, *Desalination*, 2009, **245**, 357–371, DOI: **10.1016/j.desal.2008.04.050**.

45 E. Alemayehu and B. Lennartz, Virgin volcanic rocks: Kinetics and equilibrium studies for the adsorption of cadmium from water, *J. Hazard. Mater.*, 2009, **169**, 395–401, DOI: **10.1016/j.jhazmat.2009.03.109**.

46 N. A. H. Md Nordin, S. M. Racha, T. Matsuura, N. Misdan, N. A. Abdullah Sani, A. F. Ismail and A. Mustafa, Facile modification of ZIF-8 mixed matrix membrane for CO_2/CH_4 separation: Synthesis and preparation, *RSC Adv.*, 2015, **5**, 43110–43120, DOI: **10.1039/c5ra02230d**.

47 J. D. S. F. Da Silva, D. L. Malo, G. A. Bataglion, M. N. Eberlin, C. M. Ronconi, S. Alves and G. F. De Sá, Adsorption in a fixed-bed column and stability of the antibiotic oxytetracycline supported on Zn(II)-[2-methylimidazolate] frameworks in aqueous media, *PLoS One*, 2015, **10**(6), e0128436, DOI: **10.1371/journal.pone.0128436**.

48 D. Quang Khieu, M. Thi Thanh, T. Vinh Thien, N. Hai Phong, D. Hoang Van, P. Dinh Du and N. Phi Hung, Synthesis and Voltammetric Determination of Pb(II) Using a ZIF-8-Based Electrode, *J. Chem.*, 2018, **2018**, 5395106, DOI: **10.1155/2018/5395106**.

49 Y. Zou, Y. Zhang, X. Liu and H. Zhang, Solvent-Free Synthetic Fe_3O_4@ZIF-8 Coated Lipase as a Magnetic-Responsive Pickering Emulsifier for Interfacial Biocatalysis, *Catal. Lett.*, 2020, **150**, 3608–3616, DOI: **10.1007/s10562-020-03240-w**.

50 J. Zheng, C. Cheng, W. J. Fang, C. Chen, R. W. Yan, H. X. Huai and C. C. Wang, Surfactant-free synthesis of

a Fe3O4@ZIF-8 core-shell heterostructure for adsorption of methylene blue, *CrystEngComm*, 2014, **16**, 3960–3964, DOI: **10.1039/c3ce42648c**.

51 A. Schejn, T. Mazet, V. Falk, L. Balan, L. Aranda, G. Medjahdi and R. Schneider, Fe$_3$O$_4$@ZIF-8: Magnetically recoverable catalysts by loading Fe$_3$O$_4$ nanoparticles inside a zinc imidazolate framework, *Dalton Trans.*, 2015, **44**, 10136–10140, DOI: **10.1039/c5dt01191d**.

52 J. B. Huo, L. Xu, J. C. E. Yang, H. J. Cui, B. Yuan and M. L. Fu, Magnetic responsive Fe$_3$O$_4$-ZIF-8 core-shell composites for efficient removal of As(III) from water, *Colloids Surf., A*, 2018, **539**, 59–68, DOI: **10.1016/j.colsurfa.2017.12.010**.

53 Y. Wu, B. Li, X. Wang, S. Yu, H. Pang, Y. Liu, X. Liu and X. Wang, Magnetic metal-organic frameworks (Fe$_3$O$_4$@ZIF-8) composites for U(VI) and Eu(III) elimination: simultaneously achieve favorable stability and functionality, *Chem. Eng. J.*, 2019, **378**, 122105, DOI: **10.1016/j.cej.2019.122105**.

54 Y. Zhang, Z. Xie, Z. Wang, X. Feng, Y. Wang and A. Wu, Unveiling the adsorption mechanism of zeolitic imidazolate framework-8 with high efficiency for removal of copper ions from aqueous solutions, *Dalton Trans.*, 2016, **45**, 12653–12660, DOI: **10.1039/c6dt01827k**.

55 T. Zhang, X. Zhang, X. Yan, L. Kong, G. Zhang, H. Liu, J. Qiu and K. L. Yeung, Synthesis of Fe$_3$O$_4$@ZIF-8 magnetic core-shell microspheres and their potential application in a capillary microreactor, *Chem. Eng. J.*, 2013, **228**, 398–404, DOI: **10.1016/j.cej.2013.05.020**.

56 F. Yan, Z. Y. Liu, J. L. Chen, X. Y. Sun, X. J. Li, M. X. Su, B. Li and B. Di, Nanoscale zeolitic imidazolate framework-8 as a selective adsorbent for theophylline over caffeine and diprophylline, *RSC Adv.*, 2014, **4**, 33047–33054, DOI: **10.1039/c4ra05293e**.

57 J. Q. Jiang, C. X. Yang and X. P. Yan, Zeolitic imidazolate framework-8 for fast adsorption and removal of benzotriazoles from aqueous solution, *ACS Appl. Mater. Interfaces*, 2013, **5**, 9837–9842, DOI: **10.1021/am403079n**.

58 P. Pengthamkeerati, T. Satapanajaru and P. Chularuengoaksorn, Chemical modification of coal fly ash for the removal of phosphate from aqueous solution, *Fuel*, 2008, **87**, 2469–2476, DOI: **10.1016/j.fuel.2008.03.013**.

59 K. Y. Foo and B. H. Hameed, Insights into the modeling of adsorption isotherm systems, *Chem. Eng. J.*, 2010, **156**, 2–10, DOI: **10.1016/j.cej.2009.09.013**.

60 H. Zhou, R. Bhattarai, Y. Li, S. Li and Y. Fan, Utilization of coal fly and bottom ash pellet for phosphorus adsorption: Sustainable management and evaluation, *Resour., Conserv.*

Recycl., 2019, **149**, 372–380, DOI: **10.1016/j.resconrec.2019.06.017**.

61 H. Zhang, M. Zhao and Y. S. Lin, Stability of ZIF-8 in water under ambient conditions, *Microporous Mesoporous Mater.*, 2019, **279**, 201–210, DOI: **10.1016/j.micromeso.2018.12.035**.

62 B. Kalska-Szostko, U. Wykowska, K. Piekut and D. Satuła, Stability of Fe$_3$O$_4$ nanoparticles in various model solutions, *Colloids Surf., A*, 2014, **450**, 15–24, DOI: **10.1016/j.colsurfa.2014.03.002**.

63 H. Zhang, D. Liu, Y. Yao, B. Zhang and Y. S. Lin, Stability of ZIF-8 membranes and crystalline powders in water at room temperature, *J. Membr. Sci.*, 2015, **485**, 103–111, DOI: **10.1016/j.memsci.2015.03.023**.

64 Y. Park, R. D. Whitaker, R. J. Nap, J. L. Paulsen, V. Mathiyazhagan, L. H. Doerrer, Y. Q. Song, M. D. Hürlimann, I. Szleifer and J. Y. Wong, Stability of superparamagnetic iron oxide nanoparticles at different pH values: Experimental and theoretical analysis, *Langmuir*, 2012, **28**, 6246–6255, DOI: **10.1021/la204628c**.

65 M. Shams, M. H. Dehghani, R. Nabizadeh, A. Mesdaghinia, M. Alimohammadi and A. A. Najafpoor, Adsorption of phosphorus from aqueous solution by cubic zeolitic imidazolate framework-8: Modeling, mechanical agitation *versus* sonication, *J. Mol. Liq.*, 2016, **224**, 151–157, DOI: **10.1016/j.molliq.2016.09.059**.

66 Q. Xie, Y. Li, Z. Lv, H. Zhou, X. Yang, J. Chen and H. Guo, Effective Adsorption and Removal of Phosphate from Aqueous Solutions and Eutrophic Water by Fe-based MOFs of MIL-101, *Sci. Rep.*, 2017, **7**, 1–15, DOI: **10.1038/s41598-017-03526-x**.

67 R. Liu, L. Chi, X. Wang, Y. Wang, Y. Sui, T. Xie and H. Arandiyan, Effective and selective adsorption of phosphate from aqueous solution *via* trivalent-metals-based amino-MIL-101 MOFs, *Chem. Eng. J.*, 2019, **357**, 159–168, DOI: **10.1016/j.cej.2018.09.122**.

68 J. Li, H. Chang, Y. Li, Q. Li, K. Shen, H. Yi and J. Zhang, Synthesis and adsorption performance of La@ZIF-8 composite metal-organic frameworks, *RSC Adv.*, 2020, **10**, 3380–3390, DOI: **10.1039/c9ra10548d**.

69 T. Guan, X. Li, W. Fang and D. Wu, Efficient removal of phosphate from acidified urine using UiO-66 metal-organic frameworks with varying functional groups, *Appl. Surf. Sci.*, 2020, **501**, 144074, DOI: **10.1016/j.apsusc.2019.144074**.

70 Y. Wang, W. Zhao, Z. Qi, L. Zhang, Y. Zhang, H. Huang and Y. Peng, Designing ZIF-8/hydroxylated MWCNT nanocomposites for phosphate adsorption from water: Capability and mechanism, *Chem. Eng. J.*, 2020, **394**, 124992, DOI: **10.1016/j.cej.2020.124992**.